2010

Dosimetric Effects Near Implanted Vascular Access Ports Under External Electron Beam Radiation

David Coll Segarra
Wright State University

DOSIMETRIC EFFECTS NEAR IMPLANTED VASCULAR ACCESS PORTS UNDER EXTERNAL ELECTRON BEAM RADIATION

A thesis submitted in partial fulfillment
of the requirements for the degree of
Master of Science

By

DAVID COLL SEGARRA
B.S., Montana State University, 2009

2010
Wright State University

WRIGHT STATE UNIVERSITY

SCHOOL OF GRADUATE STUDIES

September 07, 2010

I HEREBY RECOMMEND THAT THE THESIS PREPARED UNDER MY SUPERVISION BY David Coll Segarra ENTITLED Dosimetric Effects Near Implanted Vascular Access Ports Under External Electron Beam Radiation BE ACCEPTED IN PARTIAL FULFILLMENT OF THE REQUIREMENTS FOR THE DEGREE OF Master of Science

Brent D. Foy, Ph.D.
Thesis Director

Lok C. Lew Yan Voon, Ph.D.
Department Chair

Committee on
Final Examination

Brent D. Foy, Ph.D.

Michael S. Gossman, M.S., DABR

Jerry D. Clark, Ph.D.

Andrew T. Hsu, Ph.D.
Dean, School of Graduate Studies

ABSTRACT

Coll Segarra, David. M.S., Department of Physics, Wright State University, 2010. Dosimetric Effects Near Implanted Vascular Access Ports Under External Electron Beam Radiation.

Previous studies on dosimetry show important effects for metal vascular access ports for x-rays and electron beams and moderate to no effects for plastic ports for x-ray beams when ports are in the path of the beam. No previous studies exist regarding the effects of electron beams on vascular access ports other than for those made of metal although it has been suggested that electron beam attenuation through non-metal ports may be possible. Measurements of relative ionization through the device and adjacent to the device anteriorly and laterally were taken. A clinical particle accelerator delivered typical clinical electron beams of 6, 9, 12, 16, and 20 MeV through the devices. Results showed a noticeable increase in attenuation in the presence of ports, especially for lower energy beams and little or no variation in scattering measurements.

TABLE OF CONTENTS

Page

TABLE OF CONTENTS (Cont.)

Page

TABLE OF CONTENTS (Cont.)

Page

LIST OF FIGURES

Figure Page

LIST OF FIGURES (Cont.)

Appendix

Figure Page

LIST OF FIGURES (Cont.)

LIST OF FIGURES (Cont.)

Figure Page

LIST OF TABLES

Table Page

ACKNOWLEDGMENTS

I would like to acknowledge and thank Professor Michael Gossman for all of his help and guidance mentoring this project as well as allowing me to use his facility, and for being readily available anytime to answer questions. Without his help this project would have not been possible.

Finally, I would also like to thank my other committee members Dr. Brent Foy, who was also my thesis advisor, and Dr. Jerry Clark for their guidance and support through this project.

I. INTRODUCTION

Vascular access ports are widely used in medicine. A vascular access port is an implantable device used for patients who need a successive series of injections or blood sample tests. They are composed of a portal body and an attached catheter and are usually implanted in the upper chest with the catheter attached usually to the subclavian vein. Radiation oncologists often find it difficult to address clinical situations when these devices are in the way or targeting a tumor.

According to the President of the Ohio River Valley Chapter of the American Association of Physicists in Medicine, "Of approximately 600 new patients per year seen in a moderately sized radiation oncology center, a radiation oncologist may see about eight patients per year with a vascular access port implanted in an anatomical location that presents as an obstacle for treatment" [1]. Although this is only about a 1.3% incidence of occurrence, the consequence of dealing with such a case without published dosimetry guidance is crucial to the care of the patient.

When presented with a task to treat patients that have been prescribed an implantable cardioverter-defibrillator or implantable pacemaker, there exists many options for the radiation oncologists to consider; four of which are to (1) decline to treat altogether at the risk of causing detriment to the device, (2) treat only after communications with the implanting physician with agreed consideration to remove the device temporarily and prior to irradiation, (3) treat with the device intact while integrating ordinary geometries and with a reduced prescription dose to satisfy the device

dose limit or (4) treat with the device intact, however utilizing non-ideal beam arrangements to avoid the device entirely [1,2]

The first study of the dosimetric effects of x-rays and electron beams when those ports are in the path of the beam were conducted by Bagne et al. in 1990. The ports available at that time were made mostly of titanium or steel. His group showed that there is an important decrease in dose if the port is located directly in the beam path that can be observed up to 51.5% attenuation for 9 MeV electrons. Since then, technology has improved and new generation of ports containing far more plastic than metal can now be found.

Then, in 2006 Gossman et al. studied how those new devices interfered with x-rays, detailing changes in dose through various clinical treatment planning algorithms. For locations beyond the device (i.e., after the beam passes through the device), the maximum change in dose was found to be a 16.8% in attenuation for 6 MV photons. With 18 MV x-rays also investigated, dose increases of 7.0% for back-scatter locations and 7.7% for side-scatter locations were discovered as well.

No studies have been carried out on the effects of electron beams on vascular access ports other than the studies conducted for metal ports in 1990**.** It has been suggested theoretically that electron beam attenuation through non-metal ports may be clinically feasible [3]. This study will experimentally explore the affect of having composite plastic vascular access ports in the path of a therapeutic electron beam.

II. BACKGROUND

II-1 Vascular access ports

II-1.1 Description

A vascular access port is an implantable device used for patients who need a successive series of injections or blood sample tests. Examples are frequent administration of blood products, parenteral nutrition (feeding a person intravenously), antibiotics and chemotherapy [4]. Implantable access ports have been reliable and provide minimum risk to infection. Patients can have a normal life since restriction on normal activities is minimized. Figure 1 below shows a generic vascular access port with a silicone septum for needle injection.

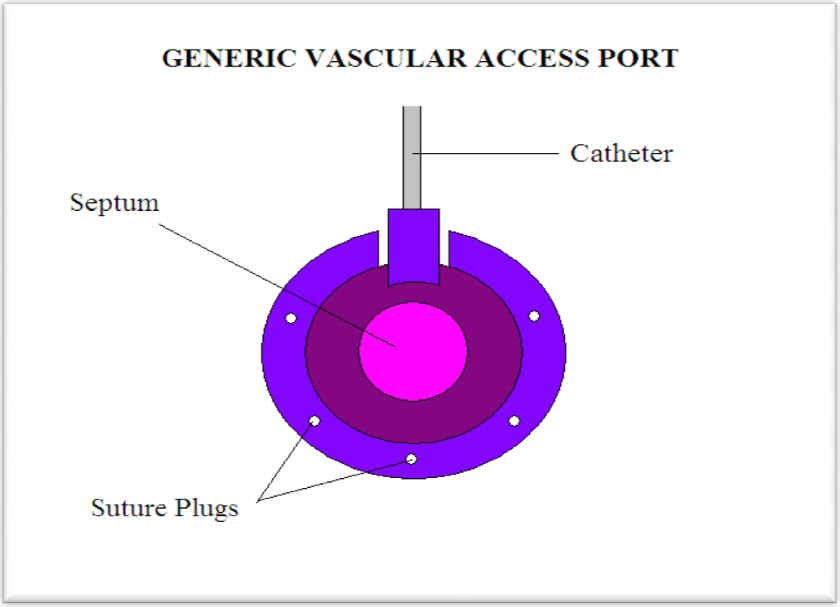

Figure 1.- Schematic of a generic vascular access port

Goodman and Wickham in 1984 wrote an overview on vascular access ports. They put together assessment criteria for identifying patients who had high priority for implant [5]. Patients who most needed vascular access ports were found to be those who had frequent venous access, long-term indefinite treatment period, continuous infusion chemotherapy, home infusion of chemotherapy, vesicant/irrigating drugs, venous thrombosis/sclerosis due to previous IV therapy, venous access limited to one extremity, prior tissue damage due to extravasation, and multiple venipunctures to secure venous access.

Now, twenty-five years later, we have a classification for vascular access port requirements. Vascular access port may now be classified as short term, intermediate term and long term for simplicity. Totally implantable vascular access ports are generally defined as those comprised of having a portal body and an attached catheter [6]. These are the devices considered for research here.

II-1.2 Previous works on vascular access ports

Studies conducted over twenty years ago by Bagne et al. [7] with several access ports composed of metal, revealed that if x-rays or electron beams were directed through it, in an attempt to target a tumor downstream, delivered dose can dramatically decrease. If the port is located directly in the beam's path, 51.5% attenuation can result for 9 MeV electrons. It was discovered that stainless steel ports attenuate more that titanium ports. This was expected due to the higher effective atomic number of the material and the greater physical density. Results from an electron beam at 6 MeV energy was not studied.

Gossman et al. [8] performed studies of attenuation, backscatter and lateral scatter in 2009 on the newest vascular access ports available to the market, with different compositions of metal and plastic and for different megavoltage x-ray energies. His group concluded that calculated doses are affected by the devices depending on composition and beam energy. Ports with more metal parts showed more effects of attenuation and scatter, whereas devices made of only plastic showed little or no effect. Attenuation of absorbed dose was as high as 16.8% for a full titanium port for 6 MV photons and 7.2% for the same port and 18 MV photons. Full plastic ports showed attenuations of only a few percent, varying from 0-4%. Backscatter measurements showed variations of 7.0% for a titanium port and 18 MV, and lateral scatter was of 7.7% for the same port same energy.

A recent study by Zhao et al. has shown that metal vascular access ports also affect dose in proton therapy [9]. Proton therapy is part of heavy ion therapy, where energies of 150-250 MeV are typically involved. The advantage of this treatment is that just after the Bragg peak (peak where dose is maximum) the dose falls almost vertically to zero. The process enables more precise dosimetry. It reduces damage to normal organs at risk.

II-1.3 Previous works on other implantable devices

Other metallic (or partially metallic) implantable devices and their effects on radiation therapy have been conducted. Gossman et al. worked with implantable peacemakers and cardio-verter defibrillators at different x-ray beam energies. His group

showed that beams can be attenuated by as much as 16%, with scatter effects at almost 6% in some cases [2].

Delacroix et al. [10] studied how the use of metal plates screwed into the bone in reconstruction of composite mandibular defects affected photon and electron beams. Those reconstructions are widely used in oral cancer therapy where patients are required to continue radiotherapy treatment after implant for some residual disease. They showed that high energy photon and electron beams interact more with the metal in the plates, causing increasing dose locally. Results from Delacroix group indicate more dramatic consequences for steel than for titanium.

Patients with a hip replacement whom go for prostate or cervical cancer treatment also created obstacles for radiation oncologists when they require brachytherapy or external beam therapy [11]. Hip prostheses are generally made of high atomic number (Z). High density alloys such as titanium, vanadium or chromium are often used. Such high Z material can produce beam hardening. Artifacts often cause CT imaging artifacts that lead to errors in computerized dose modeling. Hardening is the reduction of lower energies as the beam passes through the tissue, such that the attenuation coefficient at a depth is not the expected for the initial polychromatic beam.

Studies made by Onders et al. [12] showed that size and location are contributors to technical difficulties. An increased rate of complications such as arterial puncture, malpositions, and catheter restrictivity may appear. Surgeons now consider these associated implications prior to implanting a vascular access port.

II-2 Electron beam dosimetry

II-2.1 Introduction

An electron beam was first produced from a betatron in 1947 [13]. In the early 1950's electron beams were used in a few places for radiation therapy. In the seventies the commercialization of linear accelerators for clinical applications extended their use.

Linear accelerators use high frequency electromagnetic waves to accelerate charged particles such as electrons. Electron beams produced this way are used for superficial tumor treatment or to produce x-rays.

Clinical electron beams are of the order of 5 to 25 MeV. Electron beam therapy is good for tumors up to a depth of 6 cm. Some examples are treatment of skin, lip, head and neck cancers, or chest wall irradiation for breast cancer. Those cancers can also be treated with x-rays or radioisotopes but the main advantage of electron beam therapy is that the dose curve drops very fast beyond the treatment depth, causing minimal damage to deeper tissues. The decline is much more pronounced and closer to the surface in comparison to photons.

Electron beam therapy is very similar to photon therapy because electrons have the similar energy deposition and clinical radiobiology mechanisms than photons. However, treatment with electrons can be more focused to the desired volume with minimal effects on surrounding tissues [14]. Besides the treatment of cancers specified above, electron beam therapy can be used alone or together with photon beam therapy to treat upper respiratory and digestive tract lesions up to 5 cm in depth.

II-2.2 Electron interactions

While crossing different parts of the body electrons interact with atoms in tissues, bones, fat, and all material they find. Interactions can be either: (1) inelastic collisions with atomic electrons, (2) inelastic collisions with nuclei, (3) elastic collisions with atomic electrons, or (4) elastic collisions with nuclei.

In inelastic collisions, there is a loss of kinetic energy of the initial electron in its interaction with either an atomic electron or the nucleus. In the case of collision with an atomic electron, the energy is transferred to the final electron with a loss in the form of atom ionization or excitation. In the case of a collision with the nucleus, the loss of energy yields an x-ray. This latter interaction is called bremsstrahlung. This is a German word for 'braking' ideally suited, since the electron looses energy.

In elastic collisions there is no energy loss, as energy is conserved. Energy is either redistributed through electron-electron interactions or through electron-nucleus interactions. In some instances, the physical process involves a mere directional reorientation of the incidence electron without affecting its energy.

For all collision interactions, induced by mainly the Coulomb force, each can cause attenuation of the electron beam and degrade energy with depth until the electron is absorbed by atoms in the medium. The cross section of the electron with the medium also generates Compton scattering processes. The scattering power varies approximately as the square of the atomic number Z and inversely as the square of the kinetic energy [15]. Clinical applications require the dose to be delivered to be determinable through the

entire volume. Therefore, a high fluence of particles is needed to absorb dose to the entire volume of interest. The particle accelerator provides this needed fluence clinically.

II-2.3 Energies and dose

The dose distribution depends on the kinetic energy of the electron, so it has to be specified and determined for each beam. Brahme and Svensson in 1976 determined that the kinetic energy probable at surface $E_{p,0}$(MeV) is a function of practical range R_p(cm).

For water:

$$E_{p,0} = 0.22 + 1.98R_p + 0.0025R_p^2 \quad (1)$$

This approximation is recommended for broad beams and a source-to-surface distance (SSD) of at least 100 cm. A correction for the mean energy as a function of R_{50} (range where the energy has decreased to half of its initial value at surface) was first determined as:

$$E_0 = C_4 R_{50} \quad (2)$$

where C_4 is mostly widely accepted to be 2.33 MeV/cm. Based on this, the mean energy at a depth d is:

$$E_d = E_0(1 - d/R_p) \quad (3)$$

.II-2.4 Beam flatness and symmetry

Uniformity of the beam is required for clinical applications as well as flatness and symmetry. The characteristic flatness and symmetry profile for an electron beam is shown in figure 2 for a 6 MeV beam, 10x10 field size defined by full width at half maximum (FWHM).

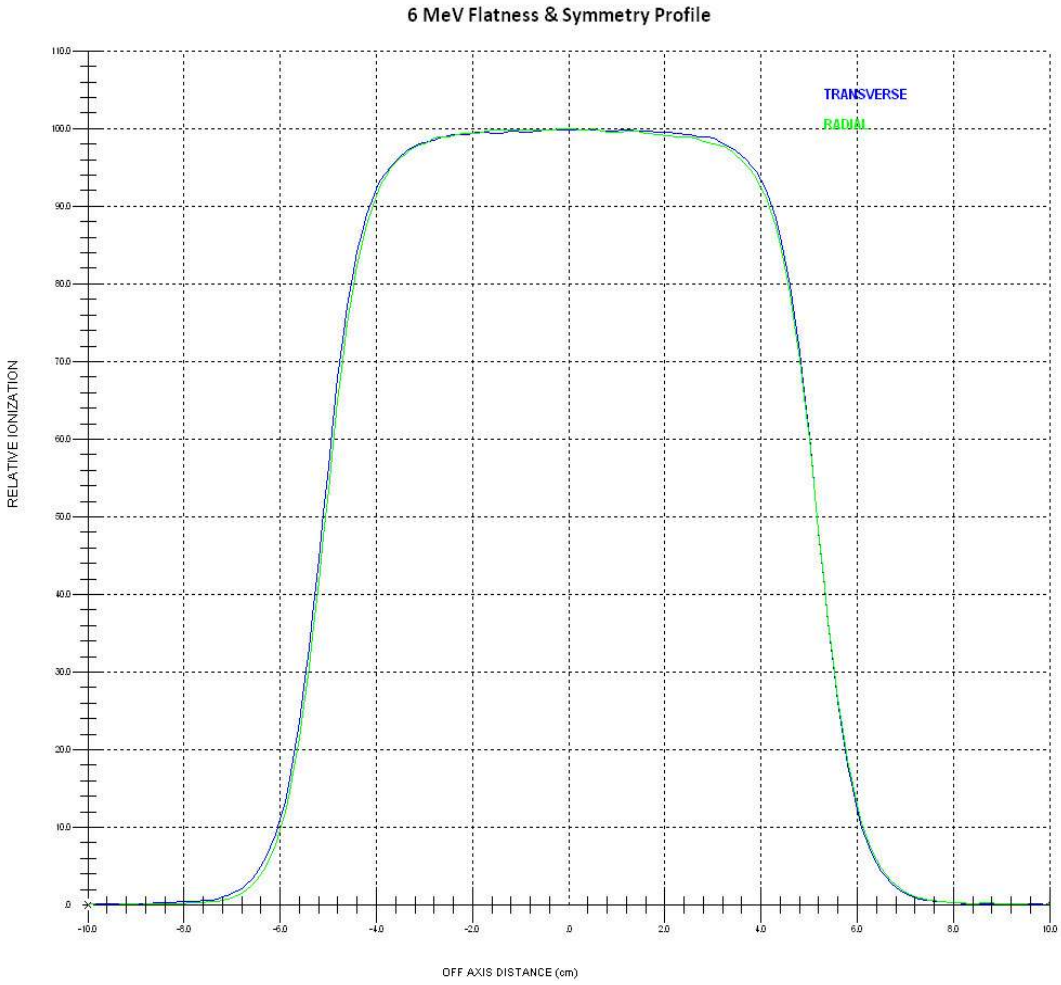

Figure 2.- 6 MeV electron beam flatness and symmetry profile

II-2.5 Absorbed dose curve

The dose at a depth is often generated for charts or graphs as a percentage of the maximum dose and can be measured with ionization chambers, silicon diodes, or film. Although calibration techniques require the use of a natural water tank, plastic media such as may be used for quality assurance testing provided the electron density of the composite plastic is approximately the same as natural water. Figure 3 shows a typical percent depth-dose standard curve for an electron beam. Changing beam energies also changes the shape of the curve displacing it to the right with higher energies and to the left with lower energies.

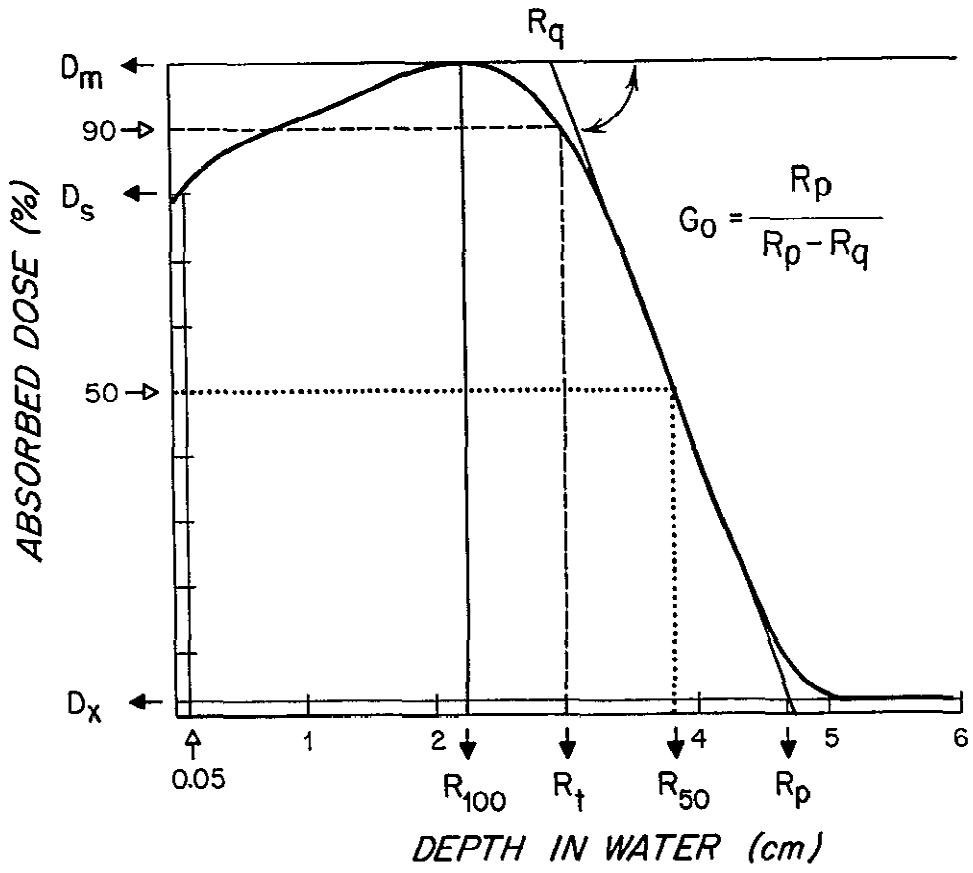

Figure 3.- Absorbed dose (%) standard curve (AAPM report # 32)

R_{100} is depth of 100% dose

R_t is therapeutic range

R_{50} is depth of 50% dose

R_p is practical range

R_q is depth of the intersection point

D_m and D_s are dose max and dose at surface

D_x is the bremsstrahlung dose

G_0 is the dose gradient

II-3 Detectors

II-3.1 Ionization chamber

An ionization chamber consists of a gas cavity separating two electrodes, the chamber wall and the center pin, connected to a high voltage power supply. Ionizing radiation creates ion pairs when entering the gas volume. When the center pin is positively charged, the negatively charged electrons created or entering are attracted to it, thus constituting a flow of charge through it. The Capintec thimble-type ionization chamber model PR-06C was used here.

II-3.2 Electrometer

An electrometer is the electronic meter connected to one of these electronic detector types. The electrometer enables the measurement of the amount of charges flowing or current level through the detector being used. Raw measurements are often used for quotient measurements, since calibration factors cancel out. Electrometers are used as a system with ionization chambers and diodes. The Capintec model 192 was used here.

II-3.3 Silicon diodes

Silicon diodes are electronic radiation measurement devices capable of being manufactured with sensitivity thousands of times the sensitivity of an air ionization chamber [13]. Diodes are ideal for quick measurements, since there is no need for voltage equilibration. The simple design of a detector diode makes it possible for these devices to be manufactured in hundreds, and positioned strategically in a water equivalent material

for multiple detections. One such array of diodes will be introduced in this research. The Sun Nuclear model MapCheck diode array was used here.

II.3.4 Film

Film is composed of a base, an emulsion, and a protective coat. The emulsion is composed of silver halide granules suspended in a gelatin mix, sensitive to visible and ultraviolet light and to ionizing radiation. Film can be used with or without intensifying screens. Film is an ideal detector of radiation dose due to its thin size. Unlike ionization chambers and diodes, which can be found 0.2-2.0 cm in width, film is less than 0.01 cm thick. Such a small device makes it suitable for close-up dosimetry. The Kodak model EDR-2 ReadyPak film media was used here.

II-4 Additional Background

II-4.1Units

The linear accelerator was calibrated such that 100 Monitor Units corresponded to 100 centiGrays (cGy). A cGy is a unit of absorbed dose and:

$$100 \text{ cGy} = 1 \text{ Gy}$$

Absorbed dose delivered to a small mass m is:

$$D(Gy) = \frac{E/m}{1\ J/Kg} \tag{4}$$

where E, the absorbed energy in Joules, is the difference between the sum of the energies of all the directly and indirectly ionizing particles which have entered the volume, and the sum of the energies of all those which have left it, minus the energy equivalent of any increase in rest mass that took place in nuclear or elementary particle reactions within the volume [16].

II- 4.2 Uncertainties

The stability of the medical accelerator for the current year was reviewed and determined to be relevant for uncertainty analysis, due to drift. Under calibration geometry; 100 cm SSD in water, a field size of 10x10 cm^2, and with the detector at the determined depth of maximum dose for each energy, a 100 MU delivery yielded fluence changes as follows in Table 1.

Ionization Chamber (Thimble) Cross-reference System

Capintec PR-06C & Capintec 192

LINA Output Drift

Month / Energy	21EX 6e	21EX 9e	21EX 12e	21EX 16e	21EX 20e
Jan	-0.4	-0.6	-0.6	-0.2	-0.9
Feb	-0.1	-0.4	-0.5	-0.3	-1.0
Mar	0.1	0.3	0.5	0.5	0.0
Apr	-0.2	0.1	0.2	0.3	-0.7
May	-0.1	0.0	-0.2	0.0	-1.0
Jun	-0.3	-0.1	-0.1	-0.2	-0.2
Average =	-0.2	-0.1	-0.1	0.0	-0.6
StdDev = +/-	0.2	0.3	0.4	0.3	0.4

T**able 1.-** Particle accelerator dose output drift for all electron energies

From the data above, all individual measurements in this research must have this included uncertainty in dose for each energy level. The uncertainty in the response of the ionization chamber and electrometer system were based on consecutive Raw readings:

Raw Reading

1. 109.2
2. 109.1
3. 109.2
4. 109.2
5. 109.1
6. 109.1
7. 109.2
8. 109.2
9. 109.2
10. 109.2

Ave = 109.2

Stdev = ± 0.1

The uncertainty in the measurements of backscatter and lateral scatter can be calculated by quadrature as shown:

6 MeV: $\sqrt{0.2^2 + 0.1^2} = 0.22$

9 MeV: $\sqrt{0.3^2 + 0.1^2} = 0.32$

12 MeV: $\sqrt{0.4^2 + 0.1^2} = 0.41$

16 MeV: $\sqrt{0.3^2 + 0.1^2} = 0.32$

20 MeV: $\sqrt{0.4^2 + 0.1^2} = 0.41$

Finally a list of consecutive readings for the diode array was also given, as determined under calibration conditions for one energy.

Raw Readings

1. 100.0
2. 100.2
3. 100.3
4. 100.8
5. 100.0
6. 99.9
7. 100.2
8. 100.2
9. 100.3
10. 100.1

Ave = 100.2

Stdev = ± 0.2

The uncertainty in the measurements of attenuation in cGy can be calculated by quadrature similarly. Note that the diode array device was not capable of providing data for 6 MeV measurements, since the device buildup material and the thickness of the underlying water phantom base total nearly 3.5 cm. This is beyond the practical range of the 6 MeV electron beam. Film was used to provide this information.

9 MeV: $\sqrt{0.3^2 + 0.2^2} = 0.36$

12 MeV: $\sqrt{0.4^2 + 0.2^2} = 0.45$

16 MeV: $\sqrt{0.3^2 + 0.2^2} = 0.36$

20 MeV: $\sqrt{0.4^2 + 0.2^2} = 0.45$

The point of location for reference on the film profile for dose to film error was precisely at the central axis. The highest value was 106 cGy while the lowest value was 103 cGy which together yield an average of 4.5% uncertainty. Film uncertainty was found to be of about 4.5% from the five measurements of no port taken in each film.

The uncertainty for 6 MeV measurements was then:

6 MeV: $\sqrt{0.4^2 + 4.5^2} = 4.51$ cGy

An additional uncertainty by location of the port and/or measurement device was estimated from the maximum distance error of about 3 mm over the entire 100 cm SSD. This error is approximated as a visual uncertainty to all measurements. This gives approximately an extra positioning error of 0.6%:

$$\text{Position uncertainty} = \left(\frac{99.7}{100}\right)^2 = 0.994 \Rightarrow 0.6\%$$

To summarize all calculations above, Table 2 was created to show all dose uncertainties.

Energy/Uncertainty	Scattering	Attenuation (MapCheck)	Attenuation (Film)
6 MeV	0.82	--	5.11
9 MeV	0.92	0.96	--
12 MeV	1.01	1.05	--
16 MeV	0.92	0.96	--
20 MeV	1.01	1.05	--

T**able 2 .-** Total uncertainties, in cGy

III. MATERIALS AND METHODS

III-1 Materials

III-1.1 Vascular access ports

Seven vascular access ports were used in this study. Each was manufactured from Bard Access Systems Inc, (Salt Lake City, UT) leader in the US market. The models chosen included the following:

1. Low Profile Titanium model 0605490
2. Rosenblatt model 0654970
3. MRI Powerport model 1808000
4. Ultra Low Profile model 0655640
5. X-port Duo model 0607650
6. Low Profile MRI model 0603880
7. Plastic Hard Base model 0604520

Figure 4 illustrates of all devices used in this study. Details of each port composition and dimensions are presented in Table 3. A close up of two devices are shown in Figure 5 for dimension relation to Table 3.

Figure 4 Vascular access ports. From left to right: Plastic Hard Base port, Low Profile MRI port, X-Port Duo, Ultra Low Profile port, MRI powerport, Rosenblatt port and Low Profile Titanium port.

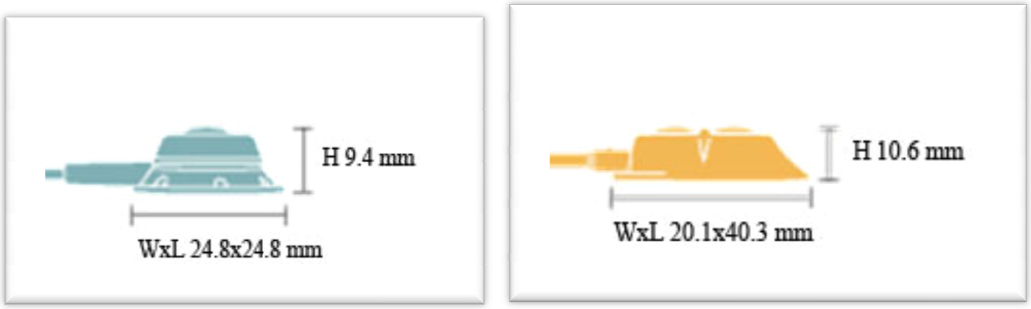

Figure 5 Sample port dimensions corresponding to the low profile titanium and the Rosenblatt models

	Low Profile Titanium	Rosenblatt	MRI Powerport	Ultra Low Profile	X-port Duo	Low Profile MRI	Plastic Hard Base
Material	Titanium	Plastic[1]	Plastic[2]	Plastic	Plastic	Plastic	Plastic
Length (mm)	24.8	40.3	30.0	22.7	38.5	24.8	32.0
Width (mm)	24.8	20.1	30.0	16.9	28.5	24.8	32.0
Height (mm)	9.4	10.6	12.9	9.2	12.6	10.0	13.5

Table 3 port material and dimensions (mm) (based on fig 4)

[1] Has a small piece of Titanium below the septa

[2] Radio Translucent

The ports used in this work are mostly made of plastic except for one made of Titanium. The Rosenblatt model has a little metal on the base. The MRI Powerport is made of radio-translucent material, so it is especially designed not to interfere with imaging techniques. The decision to choose those specific ports was made based on previous studies by Bagne et al. and Gossman et al. One metal port was chosen to corroboration of Bagne's work with electrons. Six plastic ports were chosen to extend the research done by Gossman's work with modern device designs, which was based solely on x-ray beam interactions.

The seven ports used here correspond to approximately 30% of the ports used in medicine in the United States. This calculation is based on information provided by Gossman et al. [8] where they state that their 18 ports studied from Bard Access Systems correspond to a 70% of the ports used in medicine in the United States. The seven ports used in this study are part of the 18 ports used by that group.

Dimensions of the ports used varied in length from the Ultra Low Profile port at 22.7 mm to the double-sized X-port duo and Rosenblatt models, which are about 40 mm. Width varied from the 16.9 mm diameter of the Ultra Low Profile port to the 32 mm diameter of the Plastic Hard Base port. Height varied from the 9.2 mm for the Ultra Low Profile port to 13.5 mm for the Plastic Hard Base port. Therefore, this research incorporated devices of diverse design and varying dimension.

III-1.2 Linear accelerator

The Varian Medical Systems Inc (Palo Alto, CA), Model 21EX (Trilogy) was the particle accelerator of choice. The linear accelerator (Figure 6) was used to deliver electron beams with energies of 6, 9, 12, 16 and 20 MeV. The location of the therapy machine was in Ashland, KY at the Tri-State Regional Cancer Center. For all measurements, the linear accelerator was operated at 100 monitor units with a dose-rate of 600 MU/min.

Figure 6 Varian linear accelerator

III-1.3 Detectors

MapCheck 2D silicon diode array from Sun Nuclear Corporation (Melbourne, FL) is illustrated in Figure 7. MapCheck is a 2D array of 445 diodes forming a 22 by 22 cm field size and diodes are imbedded beneath 2.0 $\pm$ 0.1 cm of water equivalency.

Figure 7.- Diode Array

The ionization chamber Freiburg model PTW TN31014 (PTW, Freiburg, Germany) is used for scatter measurements. The "pin-point" thimble-type chamber is vented and water-resistant with a sensitive volume of 0.015 cm^3. It has a build-up cap made of acrylic PMMA (Figure 8).

Figure 8.- Ionization chamber

The electrometer used to bias the chamber was a Capintec, Inc.(Ramsey, NJ) model 192. With electrometer settings of Extended Low Range, and Low Level, the center-pin of the ionization chamber received +300 V of nominal bias voltage (Figure 9).

Figure 9.- Electrometer

Kodak (Rochester, NY) Extended Dose Range EDR-2 film was chosen for use, as it is specifically designed especially for high dose-rate and high dose applications (Figure 10).

Figure 10.- Film

The ReadyPak film has low sensitivity to x-rays, making it suitable for direct, high exposures. It has a response that is approximately linear in the range from 25-400 cGy,

and a saturation exposure of 700 cGy. Dose levels were on the order of 30-100 cGy for all measurements in this study.

III-1.4 Other materials

An X-Rite (Grand Rapids, MI) model 301 transmission densitometer was required for film analysis. Absorbed dose, depicted as the darkened area after processing, reduces the amount of light passing through it. The amount of light transmission is related to the dose absorbed, where the densitometer was used to measure this optical density (OD) in a range of 0.0-5.0 OD (Figure 11).

Figure 11.- Densitometer

Film was processed using the AFP Imageworks (Elmsford, NY) Mini-Medical model 90 film processor. The processor (33”x22’x24”) has an automated design, which takes the film through the developer solution, the fixer agent, the water bath, and the drying area using rollers (Figure 12).

Figure 12.- Film processor

Plastic Water^{TM} from CIRS Inc. (Norfolk, VA) was used to calibrate photon and electron beams within a 0.5% of true water dose. The phantom media works in the range from 15 keV to 100 MeV energies. The off-white water-equivalent plastic is depicted in Figure 13.

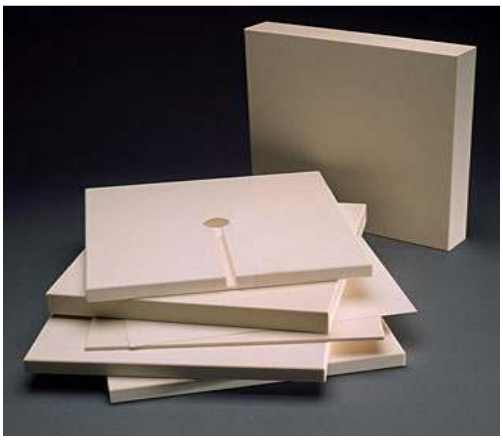

Figure 13.- Plastic Phantom

III-2 Methods

III-2.1 Electron beam percentage depth-dose curves

The percentage depth-dose curves for the Varian 21EX linear accelerator for electron beams of energies 6, 9, 12, 16 and 20 MeV are shown in Figure 14.

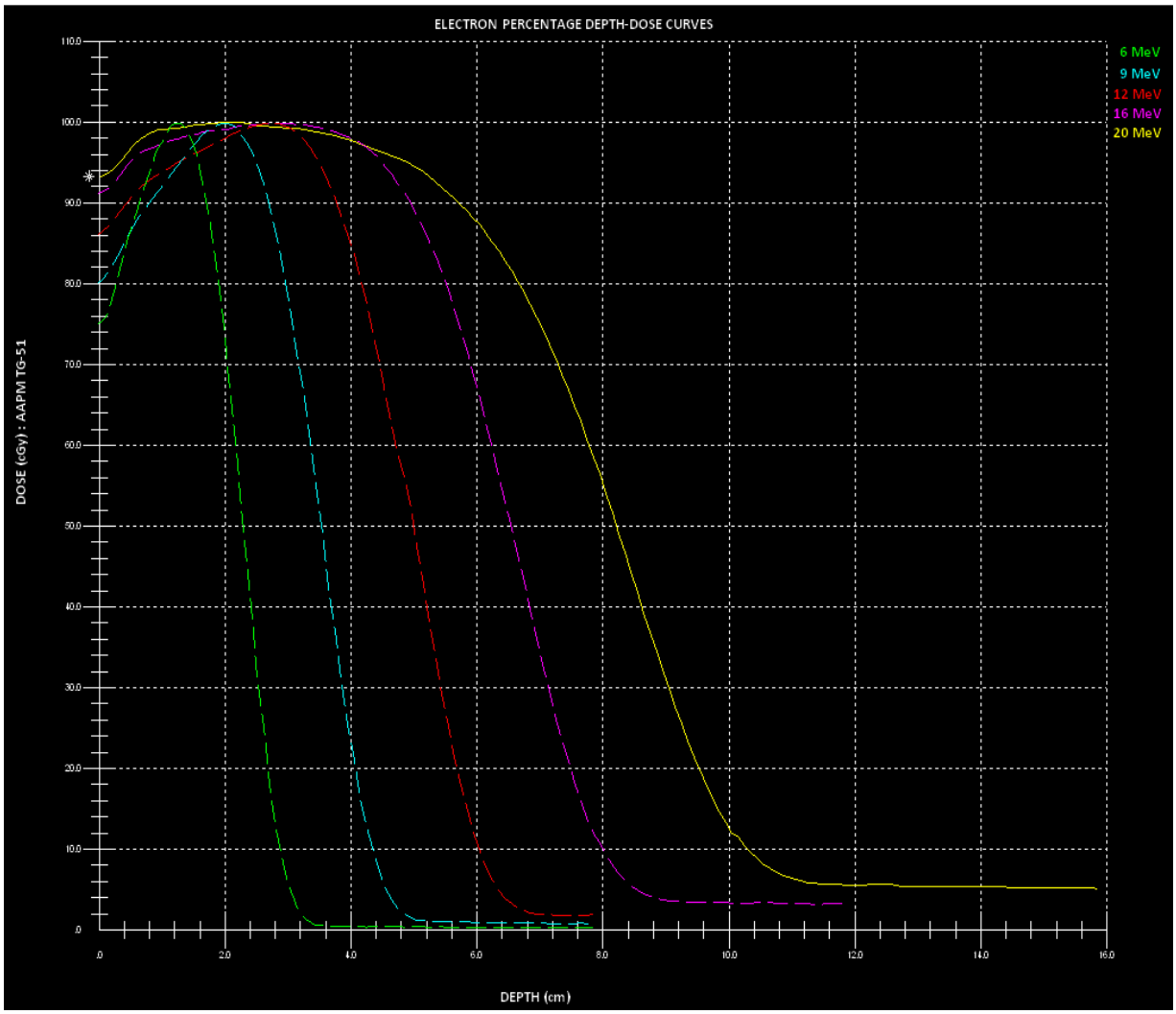

Figure 14.- Electron beam percentage depth-dose curves for the linear accelerator used These curves were used to establish the depth of water to be used as a phantom to simulate human tissue.

III-2.2 Testing Geometry for 9, 12, 16 and 20 MeV Beams

The setup consisted of a water miniature phantom of approximately 420 cm^3 made of polystyrene. It was placed on top of the MapCheck diode array. A 20x20 field size cone was attached to the gantry head for electron beam collimation (see fig 15).

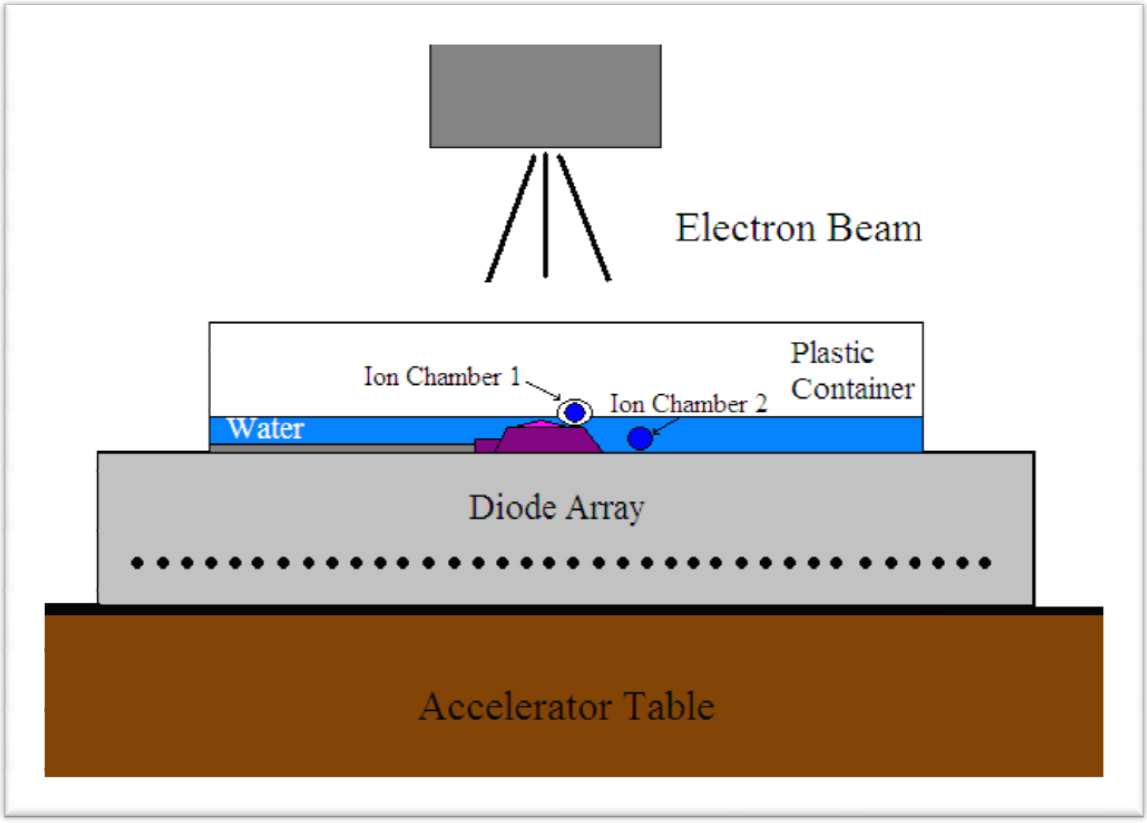

Figure 15.- Setup for 9, 12, 16 and 20 MeV. The port is inside a water container and on top of the MapCheck diode array, centered to the path of the electron beam.

A standard 100 cm source-to-surface distance was used. Natural water at 1.5 cm depth was added to completely submerge the vascular access ports. The tallest port used was 14.53 mm including the silicone septum. Due to the depth at which MapCheck diodes are imbedded in their detection plane, which is 2.0 cm downstream, the total depth of

measurement was 3.5 $\pm$ 0.1 cm. This is identified from the depth-dose curves to be adequate to achieve more than 50% of the dose, according to R_{50} in Figure 3, with the exception of the 6 MeV beam. Using this geometry, there was no need to change the method for measurement except for 6 MeV. This technique for studying this energy will be described later using film.

The MapCheck diode array was centered with the electron beam using mounted room lasers in combination with the optical distance indicator (ODI) light field projection scale. Leveling of the array was simply done using a bubble level, affixed to the MapCheck.

Ports were centered on the phantom in the direction of the beam with the catheter facing the Clinac. Relative to the graphs, the radial direction is in the direction of the table (y-axis) and the transverse direction is along the plane of linear accelerator gantry (x-axis). In order to simulate the saline solution that pulmonologists use to flush all air from the inside cavity of the vascular access port, injected water was introduced identically for all devices.

Attenuation was measured directly by the diode array device using Version 5.0 software to read the internally built electrometer. To measure lateral scatter the chamber was placed at 1 cm of the port lying on the bottom of the container. No buildup cap (see Fig. 15) was needed, since the thimble was entirely submerged. Due to its unusual non-symmetric shape, profile measurements for attenuation of the Rosenblatt port were taken in the x-direction and the y-direction.

To measure backscatter with a port in place, the chamber was positioned on top of the port. A build-up cap was then used, because the thimble it was outside of the water (lack of build-up). The distance from the ionization chamber point of measurement was chosen to be 0.3 cm, which is the cap thickness. Measurements were taken on top of the port rim, as in Figure 15.

To measure backscatter without a port in place, a total of 1.5 cm of bolus was put on the bottom of the container in order to elevate the ionization chamber at the same height when the port was present. The bolus is a tissue-like rubber material that behaves like real tissue for radiation therapy applications.

III-2.3 Testing Geometry for 6 MeV Beam

The similar setup was employed for the 6 MeV beam, however introducing film for attenuation dosimetry as shown in Figure 16.

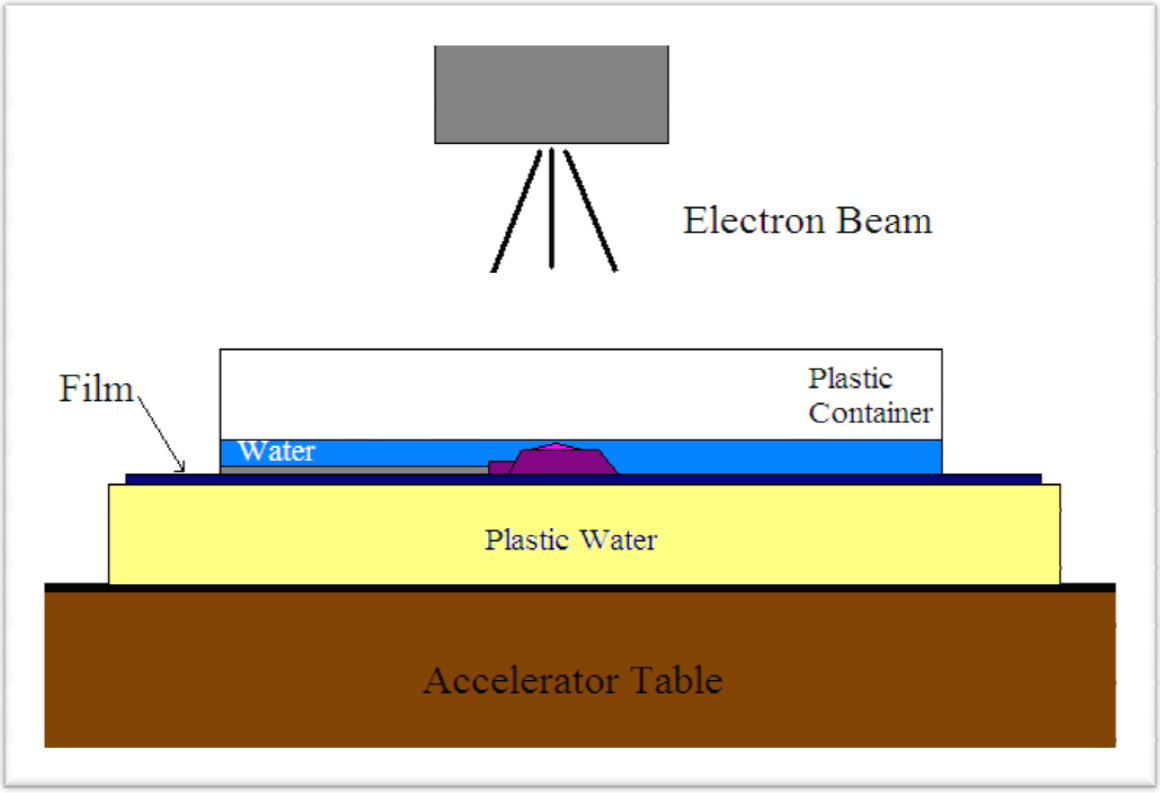

Figure 16. Setup for 6 MeV

According to Figure 14 and also to experimental data obtained from the diode array, the percent depth-dose curve for 6 MeV electrons shows that after approximately 3 cm depth there is negligible dose remaining. This was the reason why a different setup was needed. Film was the best solution due to its size and availability. However, due to changes in the granularity of film, even within the same batch, a greater uncertainty in measurement was expected.

Film was placed directly below the water phantom and on a slab of plastic phantom. Inside the phantom there was a port submerged in 1.5 cm of water and the port was filled with water to simulate the saline solution used in medicine. One film was used

for each port, and all films were from the same package to avoid possible differences in the film background fog and sensitivity.

In the measurement of 6 MeV energies the maximum changes in absorbed dose were calculated in the same way as for measurements from the MapCheck diode array. This gave a value that showed the variation with no port to the worst scenario with the port in place. As seen in the graphs, values may be higher than 100 cGy, even if they are calculated based on the calibration curve for a dose of 100 cGy. The reason for this observance is the high uncertainty of film. Uncertainties showed to be of about 7% based on measurements.

III-2.4 Calibration of Film for 6 MeV Experiments

A calibration curve was obtained by establishing the dose response to a film at different levels. Using several films with the same specifications, a total of eight films were used for the following doses (in monitor units): 100, 90, 80, 70, 60, 50, 40, 30. The linear accelerator dose rate was the same as for other energies (600 MU/min). The depth of measurement for these films were at the depth of maximum dose determined for the 6 MeV electron beam. This is nominally 1.5 cm in water. Here, the plastic phantom was used to define depth. Films were sandwiched between 1.5 cm (top) and 10 cm (bottom) Plastic Water^{TM} layers as illustrated in Figure 17.

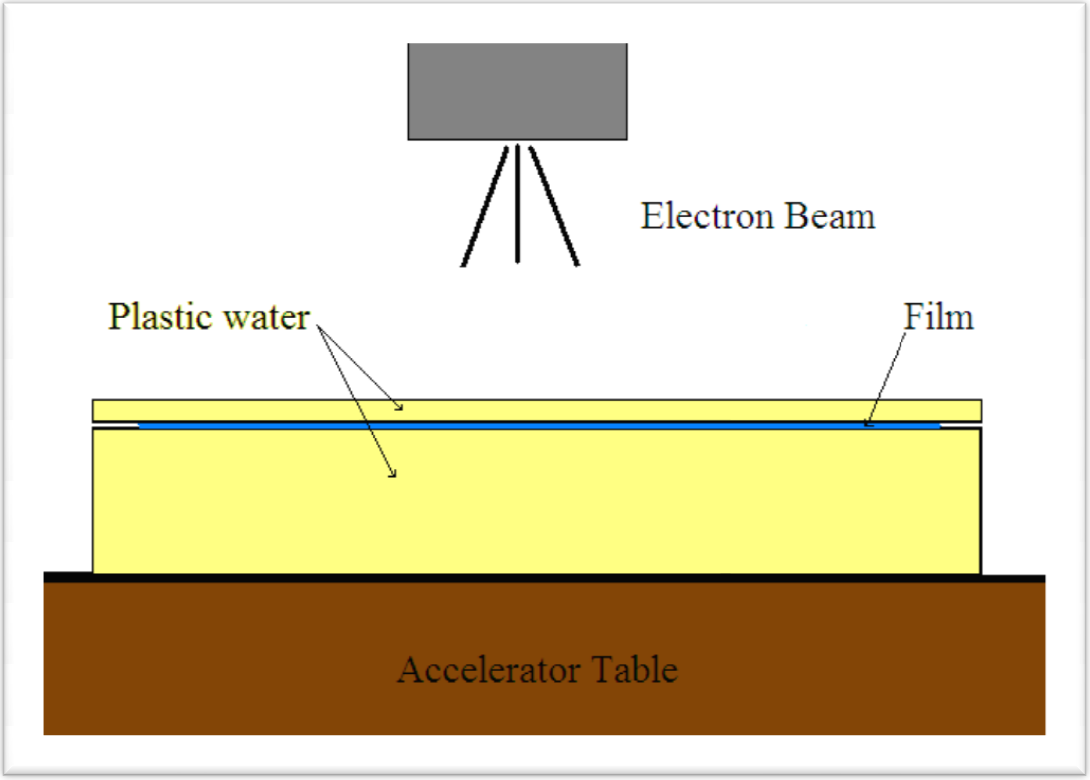

Fig 17. Setup for 6 MeV calibration curve

Once all films were irradiated, each was processed with the APF film processor. Measurements of average optical density were then read with the X-Rite transmission densitometer. Measurements were correctly reduced by base/fog measurements for each film. Base/fog is the reading of OD where the film is unexposed (clear), and is deemed equivalent to a background optical density. An H&D curve was built base on the following relationships:

From the equation of attenuation:

$$I = I_0 e^{-\mu d} \qquad (5)$$

where I is intensity of the beam at a depth d, I_0 initial intensity, μ attenuation coefficient and d depth, such that a ratio of I_0 to I can be derived as:

$$I_0/I = e^{\mu d} \qquad (6)$$

From the dose shot at the film and the OD measured, a plot of OD vs log10(Dose) can be drawn (Fig. 18)

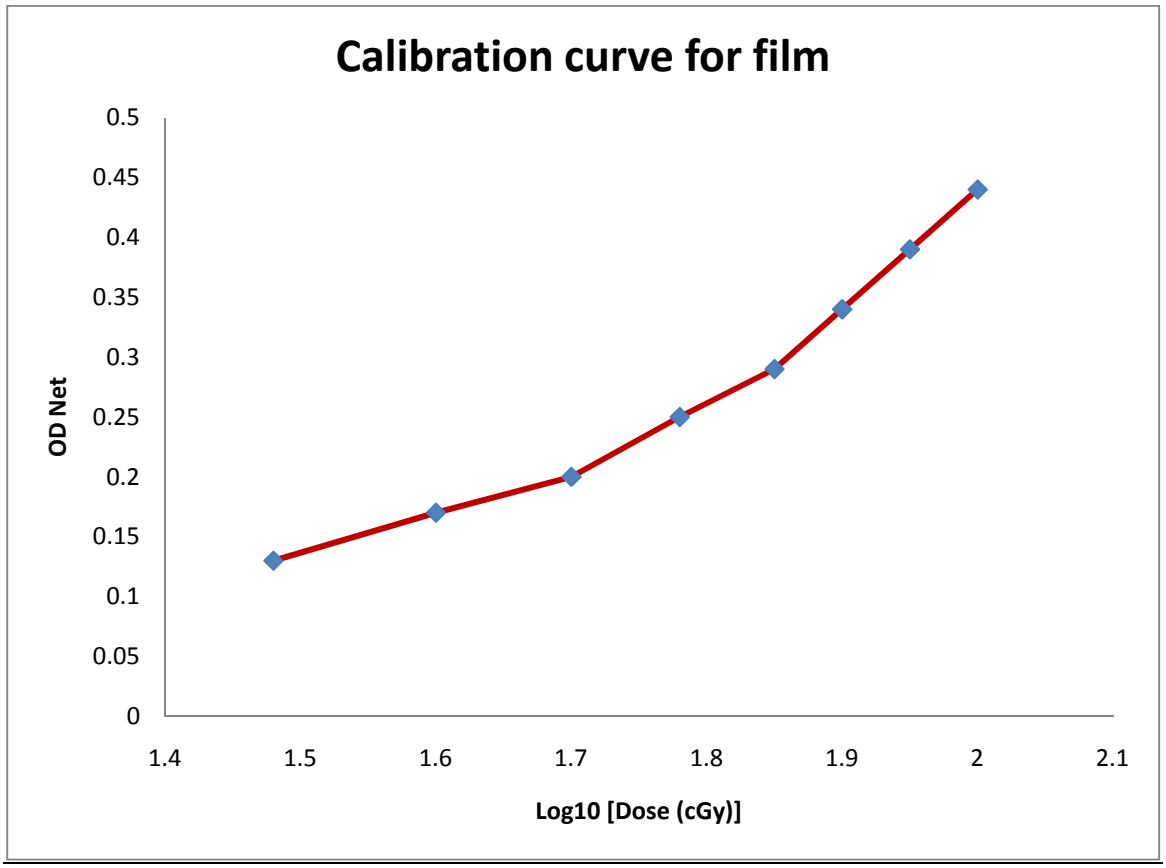

Figure 18.- Calibration curve for film Kodak EDR-2.

OD_{net} was obtained from the following equation:

$$OD_{net} = OD_{measured} - Base/fog \qquad (7)$$

Now, the net OD can be give rise to the dose absorbed to the film, by determining from the graph a corresponding $\log_{10}$(Dose). Raising the value to the power of 10 yields the dose in cGy.

III-2.5 Dose Change Calculations

III-2.5.1 Attenuation

MapCheck program was started to collect background radiation so it could be corrected later. Once the diodes detected the beam, it started collecting data. Data was saved as .txt file so it could be analyzed later with any available spreadsheet software, such Microsoft Office Excel.

From the attenuation data obtained with film and the diode array, the maximum change was determined by simple inspection on the graph by comparing the red line (no port) with the blue line (port inserted). The points with a maximum distance from the two curves give an estimate of the maximum change in dose. This identified the specific location of where to look at for scattering events as well. The maximum changes in absorbed dose were calculated from subtracting the highest value, corresponding to points far from the port, to the lowest value in the port area. The resulting values are the maximum change on absorbed dose when a port is inserted.

III-2.5.2 Lateral Scatter and Backscatter

The percent variation in both lateral scatter and backscatter was calculated using the following equation:

$$100\% \, [D_{\text{no port}} - D_{\text{port}}] / D_{\text{no port}} \qquad (8)$$

Results are tabulated in next section.

III-2.5.3 Uncertainties

From table 2 and from equations used to calculate final results, the propagated total uncertainty was calculated to be as follows:

Scattering measurements:

The worst scenario for fractional uncertainties is for the highest value v_1 and/or v_2, since both uncertainties are going to be the same:

$$\frac{\sigma v}{v} = \sqrt{(\frac{\sigma v1}{v1})^2 + (\frac{\sigma v2}{v2})^2} \quad (9)$$

This is for the case of MRI powerport, 6 MeV:

$$\frac{\sigma v}{1.8} = \sqrt{(\frac{0.82}{2.27})^2 + (\frac{0.82}{2.31})^2}$$

Total uncertainty in scattering:

$$\sigma v = 0.9\%$$

Attenuation measurements 6 MeV:

6 MeV total uncertainty = $\sqrt{5.11^2 + 5.11^2} = 7.2\%$

Attenuation measurements 9, 12, 16 and 20 MeV:

9 MeV total uncertainty = $\sqrt{0.96^2 + 0.96^2} = 1.4\%$

12 MeV total uncertainty = $\sqrt{1.05^2 + 1.05^2} = 1.5\%$

16 MeV total uncertainty = $\sqrt{0.96^2 + 0.96^2} = 1.4\%$

20 MeV total uncertainty = $\sqrt{1.05^2 + 1.05^2} = 1.5\%$

IV. RESULTS

IV-1 Lateral scatter and backscatter

A table was created for each of the ports with the measurements of lateral scatter and backscatter for each energy range. Raw readings were measured. The calculated uncertainty in measurement from the ionization chamber and electrometer system were included. The experimental uncertainty was determined unappreciable.

IV-1.1 Lateral scatter and backscatter without port

Table 4 shows the results of readings without a port.

Beam Energy (MeV)	Lateral scatter (Rdg)	Backscatter (Rdg)
6	2.27 2.27	1.98 1.98
9	2.09 2.09	1.99 1.99
12	2.16 2.16	2.12 2.13
16	2.23 2.24	2.22 2.22
20	2.23 2.24	2.23 2.24

Table 4 No vascular access port lateral and backscatter measurements

All other tables show the measurements in Raw readings and the percent change, referred to table 4.

IV-1.2 Lateral scatter and backscatter with port

Beam Energy (MeV)	Lateral scatter (Rdg)	% Variation	Backscatter (Rdg)	% Variation
6	2.27 2.28	~0	1.96* 1.96	~0
9	2.14 2.14	2.4	2.00 2.00	0.5
12	2.20 2.20	1.9	2.13 2.13	~0
16	2.26 2.26	1.3	2.22 2.22	~0
20	2.24 2.24	~0	2.23 2.24	~0

Table 5 Vascular access port Low Profile Titanium lateral and backscatter measurements

Beam Energy (MeV)	Lateral scatter (Rdg)	% Variation	Backscatter (Rdg)	% Variation
6	2.29 2.28	0.6	1.98 1.98	~0
9	2.12 2.12	1.4	2.00 2.00	0.5
12	2.18 2.18	0.9	2.13 2.13	0.2
16	2.25 2.24	0.4	2.22 2.22	~0
20	2.23 2.23	~0	2.23 2.23	~0

Table 6 Vascular access port Rosenblatt lateral and backscatter measurements

Beam Energy (MeV)	Lateral scatter (Rdg)	% Variation	Backscatter (Rdg)	% Variation
6	2.31 2.31	1.8	2.00 2.00	1.0
9	2.15 2.15	2.9	2.01 2.01	1.0
12	2.19 2.19	1.4	2.15 2.15	1.2
16	2.26 2.26	1.1	2.24 2.24	0.9
20	2.24 2.24	0.2	2.25 2.25	0.9

Table 7 Vascular access port MRI Powerport lateral and backscatter measurements

Beam Energy (MeV)	Lateral scatter (Rdg)	% Variation	Backscatter (Rdg)	% Variation
6	2.30 2.30	1.3	1.98 1.98	~0
9	2.13 2.13	1.9	2.00 2.00	0.5
12	2.18 2.18	0.9	2.13 2.13	0.2
16	2.25 2.25	0.8	2.22 2.23	0.2
20	2.25 2.24	0.4	2.24 2.24	0.4

Table 8 Vascular access port Ultra Low Profile lateral and backscatter measurements

Beam Energy (MeV)	Lateral scatter (Rdg)	% Variation	Backscatter (Rdg)	% Variation
6	2.30 2.30	1.3	2.00 2.00	1.0
9	2.13 2.13	1.9	2.00 2.00	0.5
12	2.18 2.18	0.9	2.13 2.14	0.5
16	2.25 2.25	0.7	2.23 2.23	0.5
20	2.24 2.24	0.2	2.24 2.25	0.7

Table 9 Vascular access port X-port Duo lateral and backscatter measurements

Beam Energy (MeV)	Lateral scatter (Rdg)	% Variation	Backscatter (Rdg)	% Variation
6	2.29 2.29	0.9	1.98 1.98	~0
9	2.12 2.12	1.4	2.00 2.01	0.8
12	2.17 2.17	0.5	2.13 2.13	0.2
16	2.24 2.25	0.4	2.23 2.23	0.5
20	2.24 2.24	0.2	2.24 2.24	0.4

Table 10 Vascular access port Low Profile MRI lateral and backscatter measurements

Beam Energy (MeV)	Lateral scatter (Rdg)	% Variation	Backscatter (Rdg)	% Variation
6	2.30 2.30	1.3	1.99 1.98	0.3
9	2.13 2.13	1.9	2.01 2.01	1.0
12	2.18 2.18	0.9	2.14 2.14	0.7
16	2.25 2.25	0.7	2.23 2.24	0.7
20	2.24 2.24	0.2	2.25 2.25	0.9

Table 11 Vascular access port Plastic Hard Base lateral and backscatter measurements

It is noteworthy that Table 4 (no port) results show 1.98 Rdg for backscatter at 6 MeV. It was expected that 1.96 Rdg result or even slightly less, based on measurements with the metal port. The Low Profile Titanium (metal port) gave 1.96 Rdg for this energy, so without any port present backscatter was expected to be lower. There was significant variation of affect for most electron energies regarding the metal port (Low Profile Titanium).

In general, the greatest variation in lateral scatter is for lower energies, 6 and 9 MeV. A more bulky port design seems to have a greater impact on changes in scattering than the material of the device.

Backscatter does not seem to be very significant, with higher values around only 1%. However, see the attenuation profiles below using higher energies (16 to 20 MeV).

IV-2 Attenuation

Figure 14 earlier showed R_{50} for all energy ranges and it showed that for a 6 MeV beam at approximately 3.5 cm there is only available about 2 or 3% of the dose that corresponds to the tail caused by bremsstrahlung effects, so graphs were obtained from film measurements. Graphs were obtained for 9, 12, 16 and 20 MeV from MapCheck measurements.

For 9 MeV electrons dose showed a continuous value of approximately 60% for all the length of the container and is consistent with the calibration curve. The profile of 12, 16 and 20 MeV electrons without a port showed a horizontal line at approximately 85% which is a lower value than the one expected from observing the calibration curve (100%). The explanation could be that the 2 cm depth added by the MapCheck diode array is plastic, and plastic does not behave exactly as water, so attenuation is a little higher.

A graph was created for each electron energy with both curves: with port represented with a red line and without port, represented with a blue line to visually compare the difference. Representative sample graphs are shown below. The 6 MeV profile for the Low profile titanium shows the maximum attenuation of all the cases studied here (Figure 19). For all the graphs obtained the absorbed dose without a port is a red line and the absorbed dose in the presence of a port is a blue line.

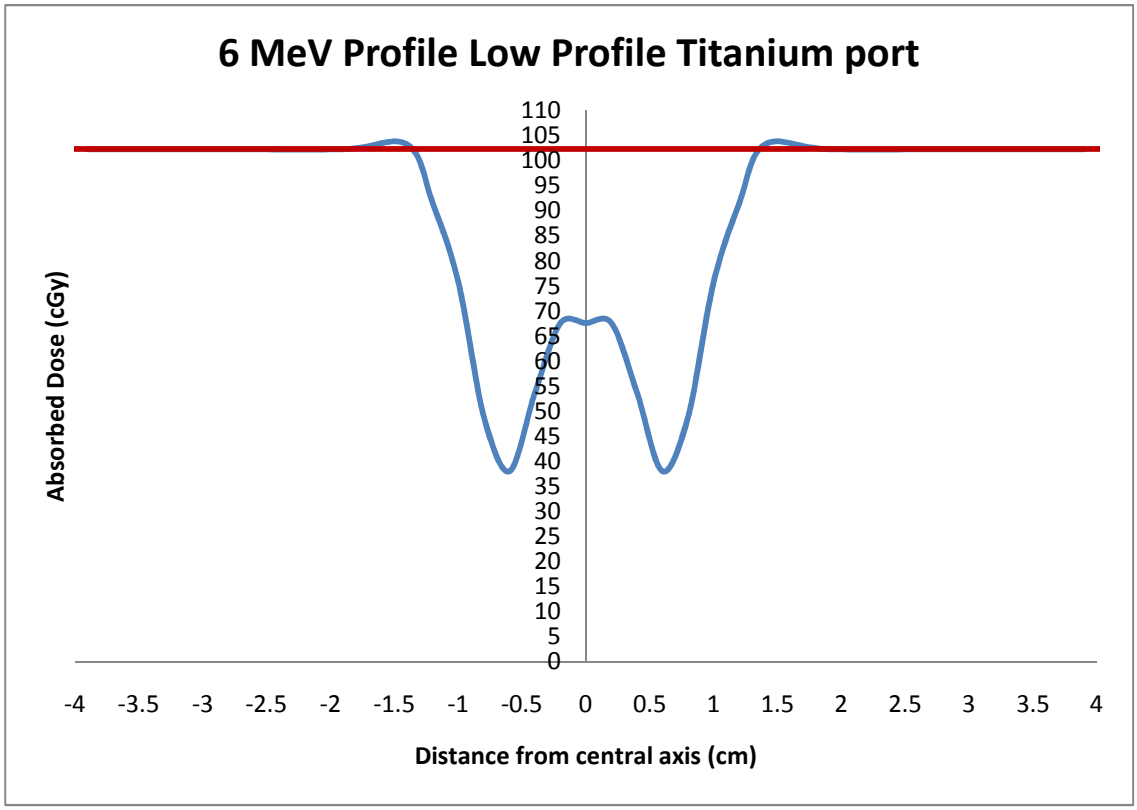

Figure 19 Low Profile Titanium port 6 MeV

It can be clearly distinguished the two peaks of lowest dose where there is more metal, and in the middle there is less attenuation because there is the silicone septum. Figure 20 shows an increase of dose in the immediate surroundings of the port and was observed mostly in ports with metal parts at high energies (16 and 20 MeV)

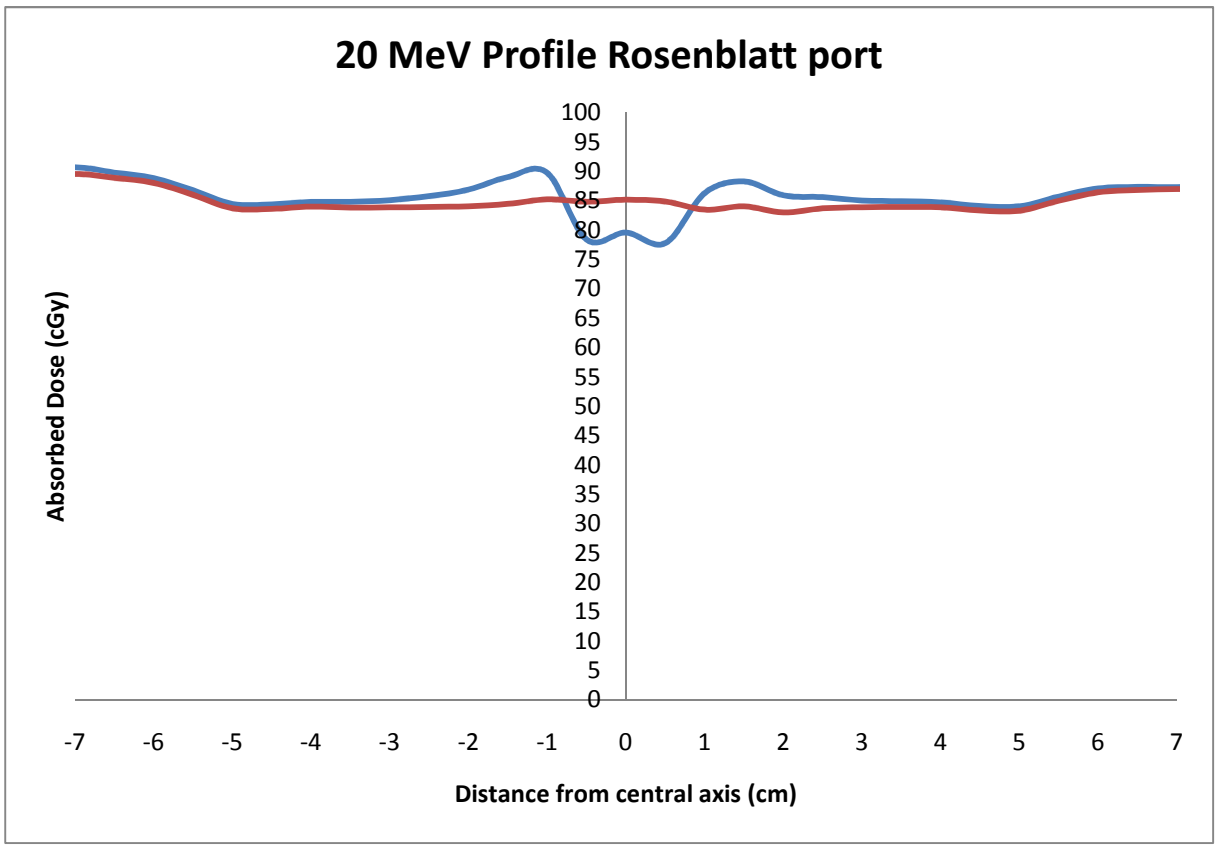

Figure 20 Rosenblatt port 20 MeV Y-axis

Graphs for all ports at all energies can be found in the appendix of this document. As described in the Materials and Methods section, the maximum dose attenuation for each combination of port and beam energy was calculated. These results are shown in Table 12 below.

Attenuation (%)	6 MeV	9 MeV	12 MeV	16 MeV	20 MeV
Low Pro Titanium	**62 ± 7.2%**	**32 ± 1.4%**	**27 ± 1.5%**	**20 ± 1.4%**	**21 ± 1.5%**
Rosenblatt	**49 ± 7.2%**	**23 ± 1.4%**	**21 ± 1.5%**	**16 ± 1.4%**	**16 ± 1.5%**
MRI Powerport	**16 ± 7.2%**	**15 ± 1.4%**	**9 ± 1.5%**	**5 ± 1.4%**	**4 ± 1.5%**
Ultra Low Profile	**6 ± 7.2%**	**8 ± 1.4%**	**4 ± 1.5%**	**3 ± 1.4%**	**1 ± 1.5%**
X-Port Duo	**15 ± 7.2%**	**9 ± 1.4%**	**5 ± 1.5%**	**4 ± 1.4%**	**3 ± 1.5%**
Low Profile MRI	**6 ± 7.2%**	**5 ± 1.4%**	**2 ± 1.5%**	**2 ± 1.4%**	**1 ± 1.5%**
Plastic Hard Base	**7 ± 7.2%**	**9 ± 1.4%**	**4 ± 1.5%**	**3 ± 1.4%**	**2 ± 1.5%**

Table 12.- Electron beam attenuation (%) for each port

The port that showed the greatest attenuation was the Low Profile Titanium port, with dose reductions by as much as 62% for 6 MeV electrons. This was expected since this is the metal port. The Rosenblatt port that is made of plastic with a small piece of metal below the septa showed surprising results. Dose attenuation can reach 49% for 6 MeV and for higher energy (20 MeV) attenuation has still a maximum of 16%. The rest of the ports are made of plastic and results are still noticeable. The MRI Powerport and the X-port Duo, both of considerable size, showed maximum attenuations of about 16% for 6 MeV. All other ports showed maximums of less than a 10% in all cases.

V. DISCUSSION

Seven vascular access ports were studied using five different electron beam energies. Measurements of attenuation, lateral scatter and backscatter were taken. Results showed that lateral scatter from a vascular access port for electron beams can alter expected dose by as much as 2.9%, while expected dose in the backscatter direction can change by a maximum of 1.2%. A probability test of the value within uncertainties of being non-zero was conducted with the Matlab^{TM} function 'normcdf' and the minimum value acceptable was found to be 1.48%. This function was used to find the minimum value that, with an uncertainty of 0.9, has a probability of 95% or more of not being zero. That test concluded that all values of scattering with a variation of 1.48 or less are statistically irrelevant.

Two attenuation profiles revealed an increase in the dose in the immediate surroundings of the port for 16 and 20 MeV. This increase was about 5% in the two ports containing some metal (Low Profile Titanium and Rosenblatt). This may be related to the finding from a study on mandibular reconstruction [10] that revealed an increase in dose in the vicinities of the metal parts for MeV range photon and electron beams. Similar results are found here. While the ion chamber was 1 cm laterally to the port, the diodes in Mapcheck are 2 cm below the plane of the port, were lateral scatter due to bremsstrahlung effects can be higher (Fig. 21).

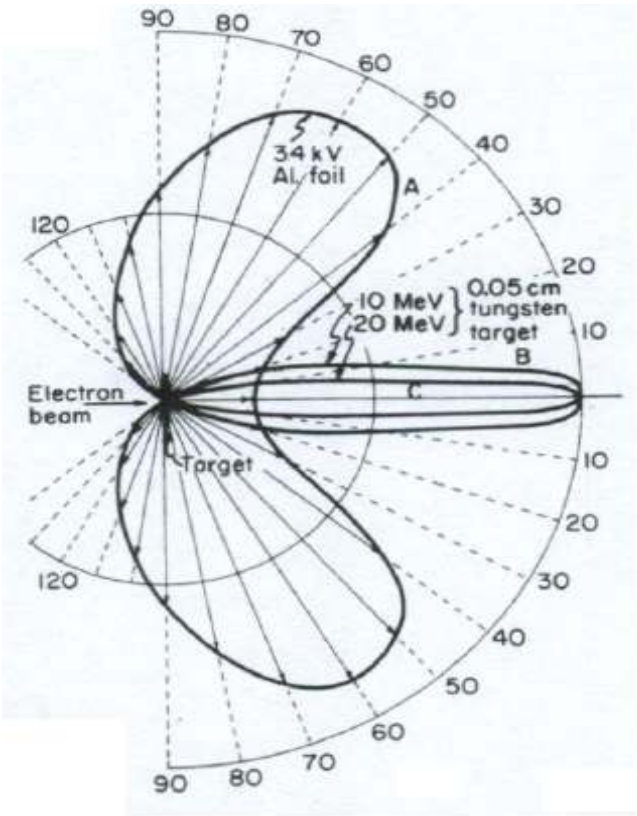

Polar diagram showing intensity variation from x-rays produced at a specific angle.

Figure 21.- Lateral scatter from an electron beam due to bremsstrahlung effects [17]

Graphs showed a noticeable increase in attenuation for lower energy beams. In the case of port the Low Profile Titanium port it showed the expected behavior from Bagne's work [7]. Attenuation maxima were of about 60% for 6 MeV electrons and about 20% for 16 and 20 MeV electrons.

Results in attenuation, backscatter and lateral scatter show a decreasing behavior in the order that ports are presented in this study in a similar way as they did in Gossman's work with x-rays [8] but this time effects were considerable for most of the ports at low energies. This order starts with metal ports, mixed ports and ends with full plastic ports.

Plastic ports showed increasing attenuation according to the size or apparent quantity of plastic involved.

Some results, as already shown in the Results section reveal that the greatest attenuation was the low profile titanium port, with dose reductions by as much as 62% for 6 MeV electrons. The Rosenblatt port showed dose attenuation of 49% for 6 MeV and for higher energy (20 MeV) attenuation has still a maximum of 16%. Since this port has a small piece of metal in the base, and results for all plastic ports are far below these numbers, it should be concluded that any port with a mix of plastic and metal should be treated with caution when calculating dose.

The rest of the ports are made of plastic and results are still noticeable. The MRI Powerport and the X-port Duo, both of considerable size, showed maximum attenuations of about 16% for 6 MeV. All other ports showed maximums of less than a 10% in all cases. The statistical significance of the results was determined by the level of uncertainty and the resulting variation.

It is concluded that, (1) for 12 and 20 MeV with a 1.5 % uncertainty, variations of less than 2.47 % are statistically insignificant, (2) For 9 and 16 MeV with a 1.4% uncertainty, variations of less than 2.31% are statistically insignificant, (3) for 6 MeV with a 7.2% uncertainty, variations of less than 11.9 are statistically insignificant.

In conclusion, therapeutic medical physicists should be aware of the impact metal and plastic vascular access ports have on high energy electron beams. The levels of attenuation should be specifically cautioned to radiation oncologists as they consider treatment through these devices. When identified as a clinical barrier, consultation with

the implanting physician should be sought after, where options for port relocation or removal may be possible. Otherwise, the date collected in this research may be used as a reference to assist medical physicists in the validation of computerized dose modeling for prescribed radiation therapy treatment delivery.

VI. APPENDIX

Port 1: 0605490 Low Profile Titanium

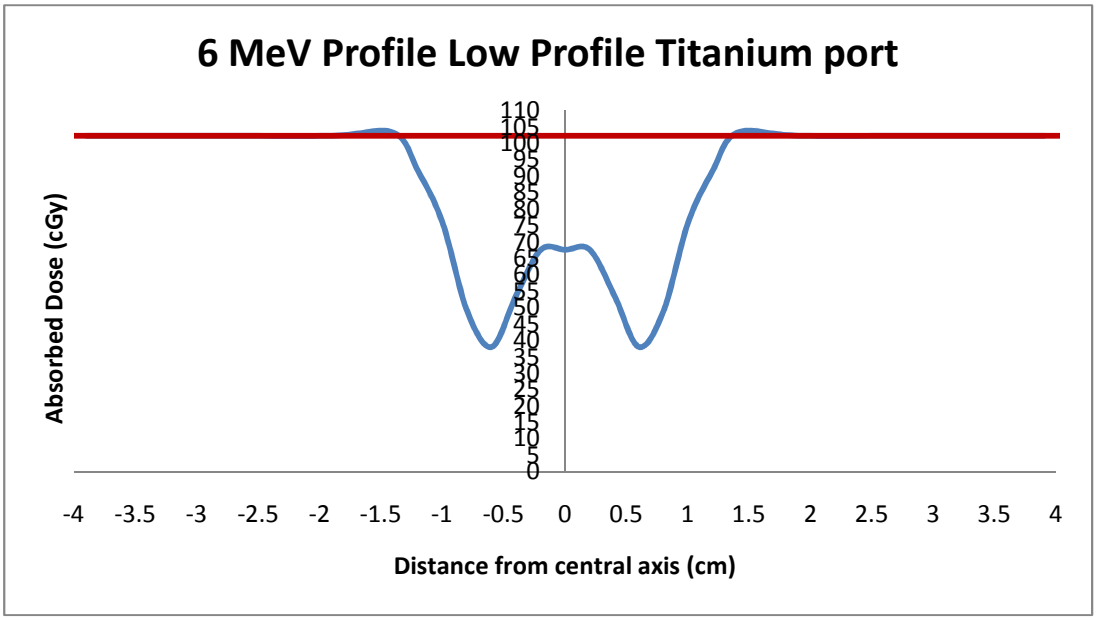

Figure 22 Low Profile Titanium Port 6 MeV

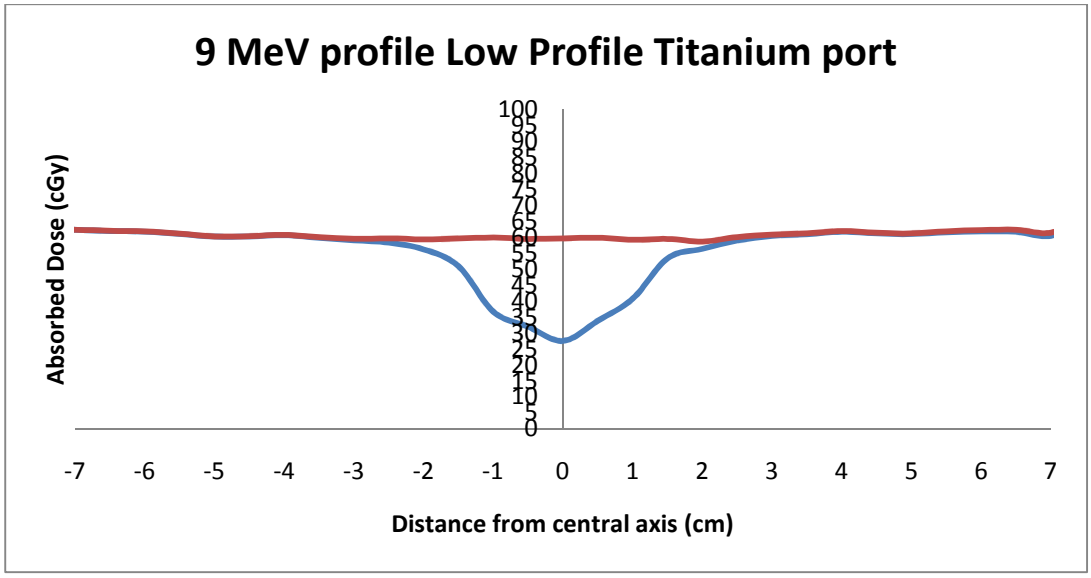

Figure 23 Low Profile Titanium Port 9 MeV

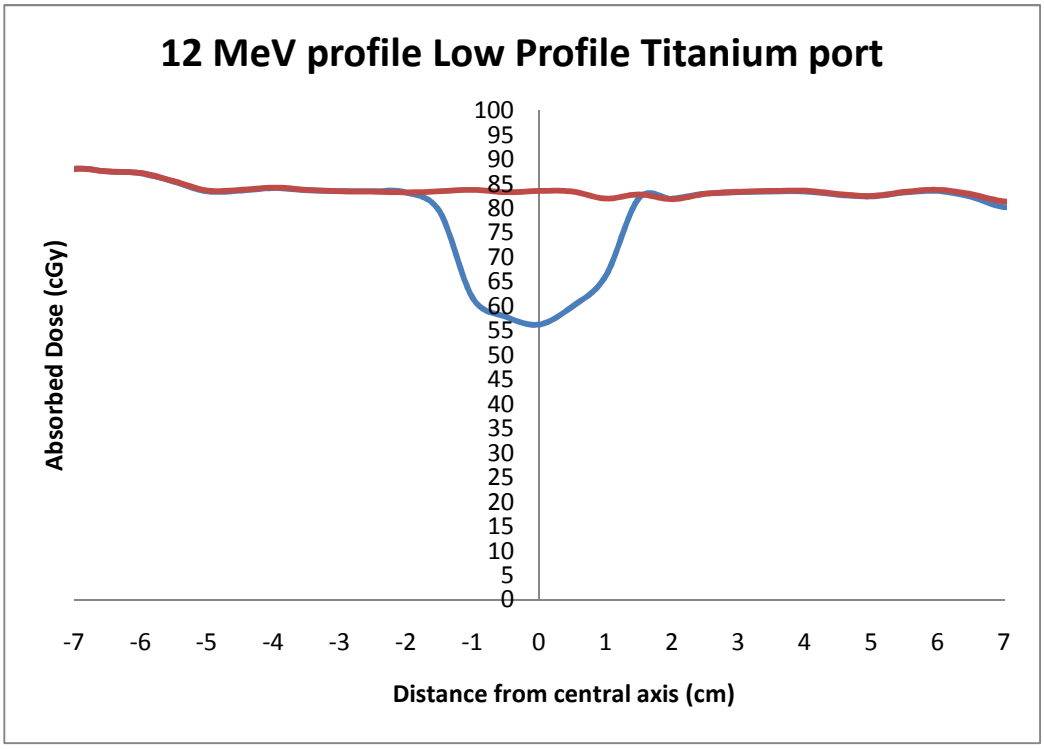

Figure 24 Low Profile Titanium Port 12 MeV

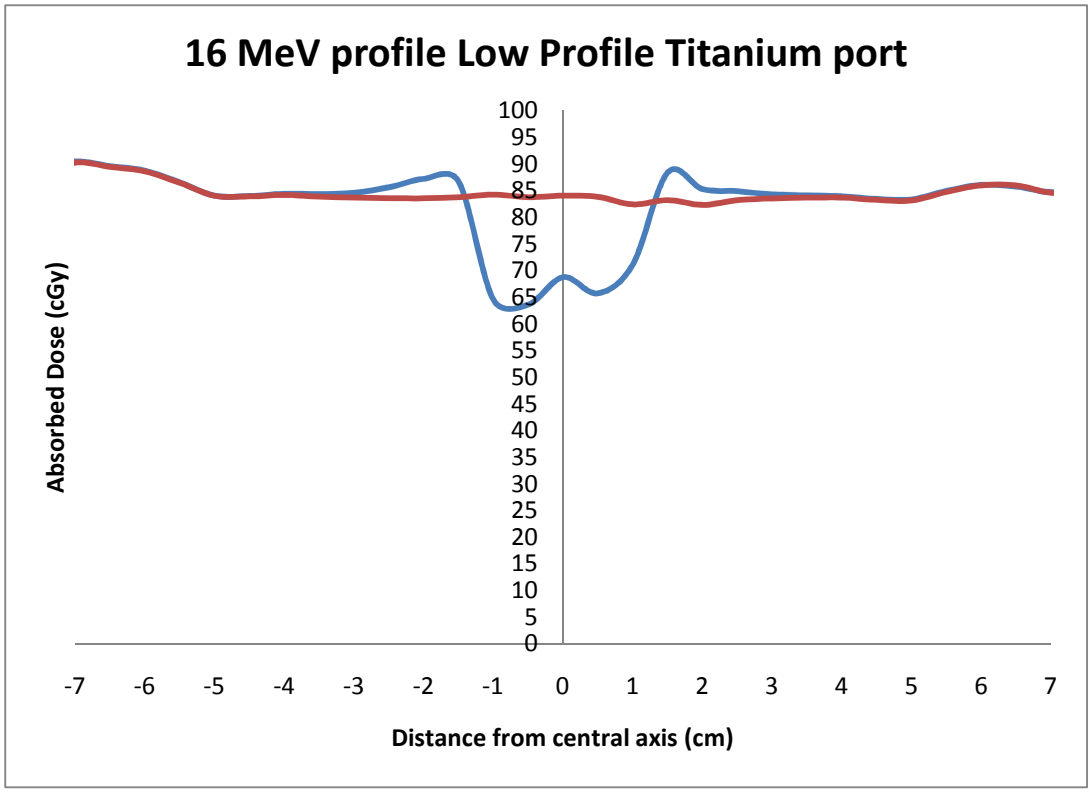

Figure 25 Low Profile Titanium Port 16 MeV

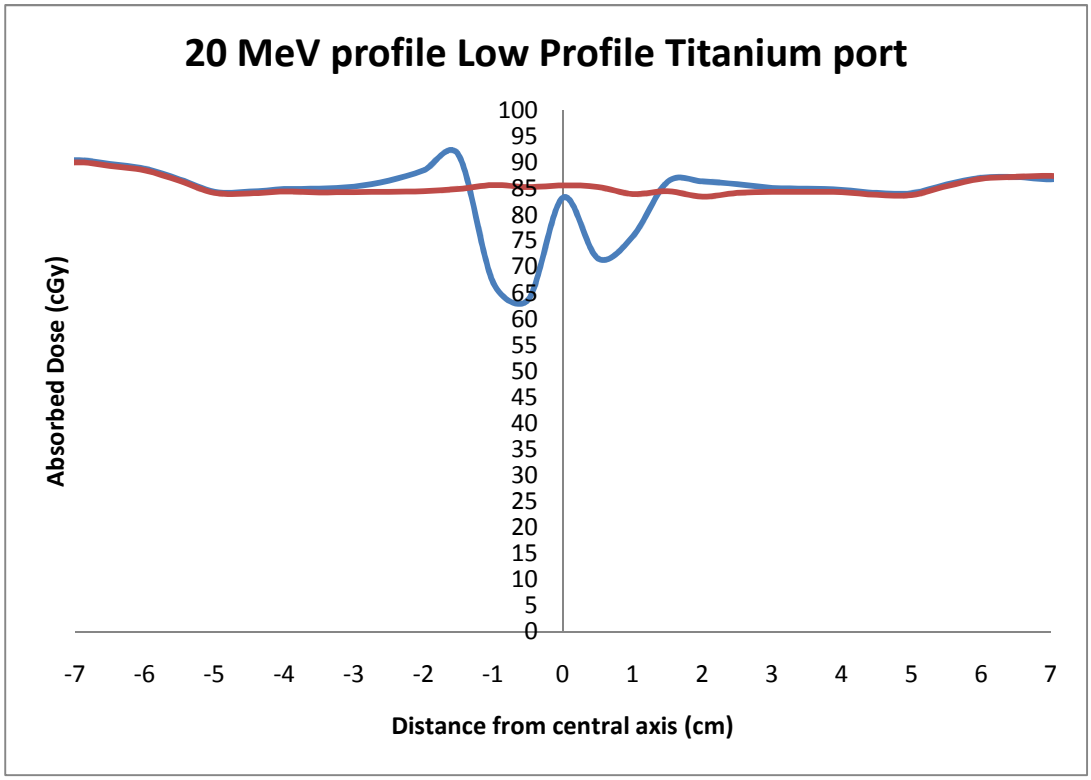

Figure 26 Low Profile Titanium Port 20 MeV

Port 2: 0654970 Rosenblatt

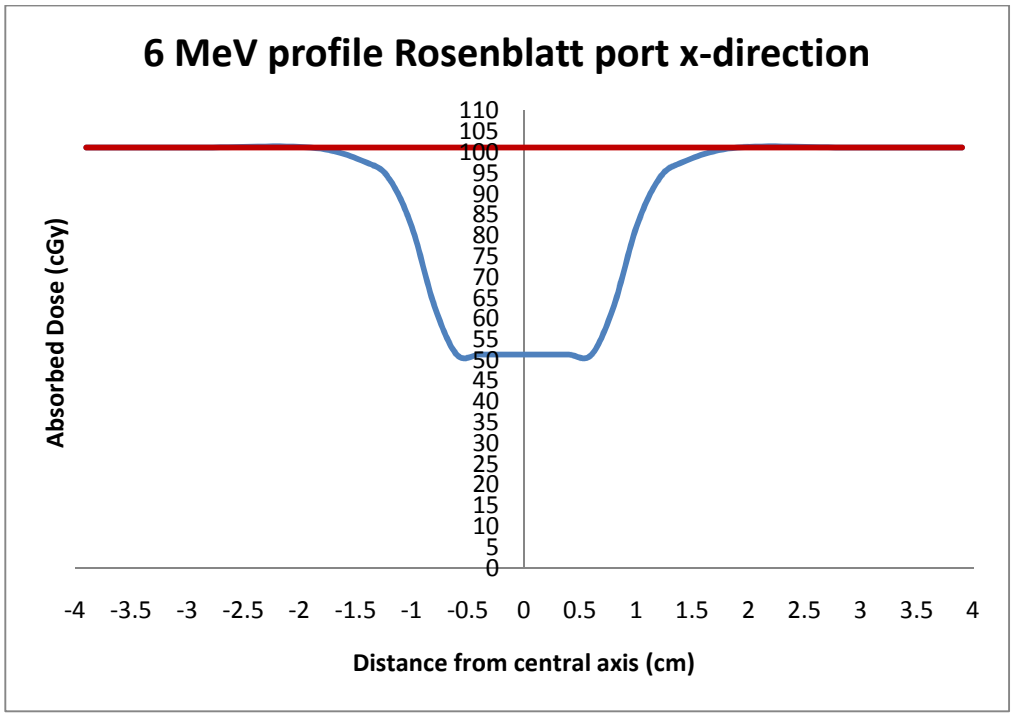

Figure 27 Rosenblatt Port 6 MeV X-axis

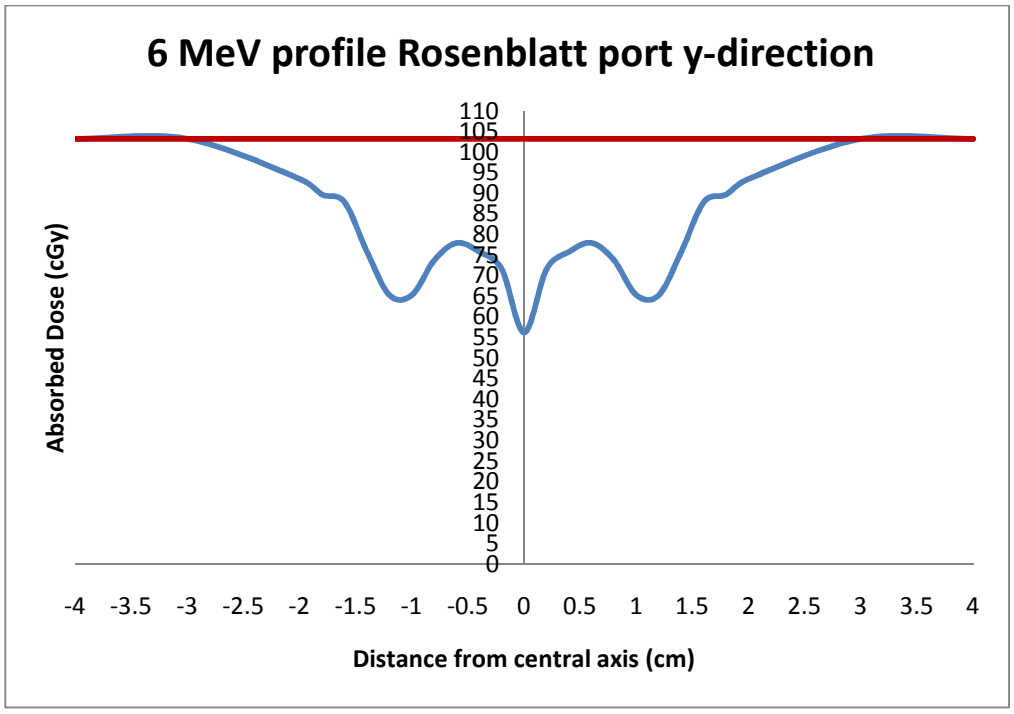

Figure 28 Rosenblatt Port 6 MeV Y-axis

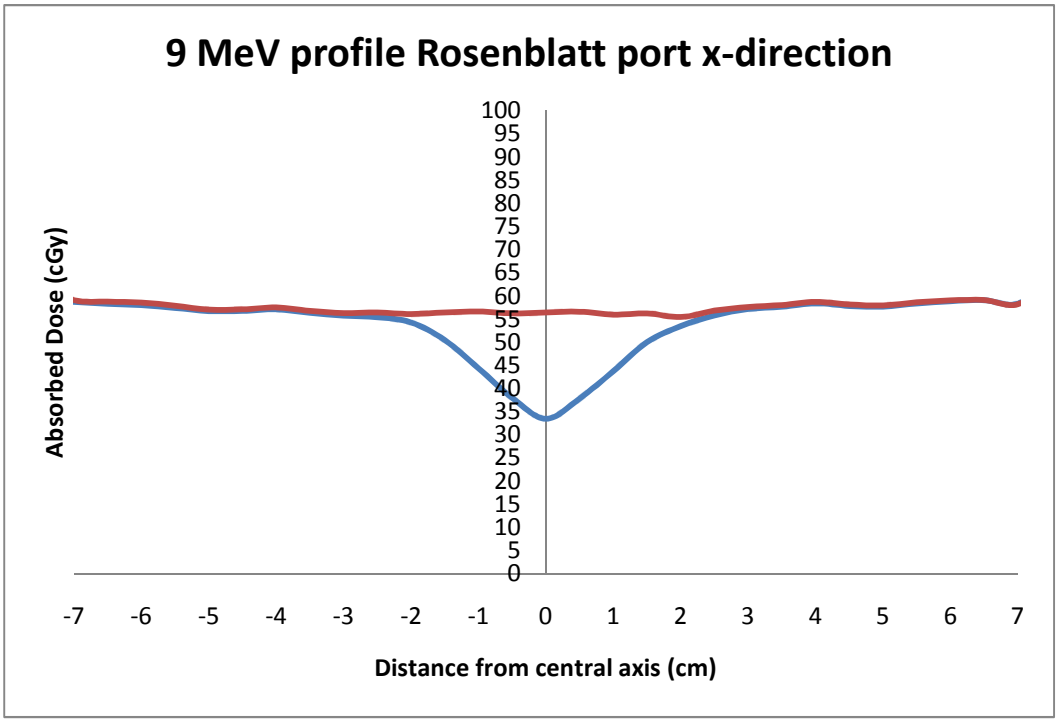

Figure 29 Rosenblatt Port 9 MeV X-axis

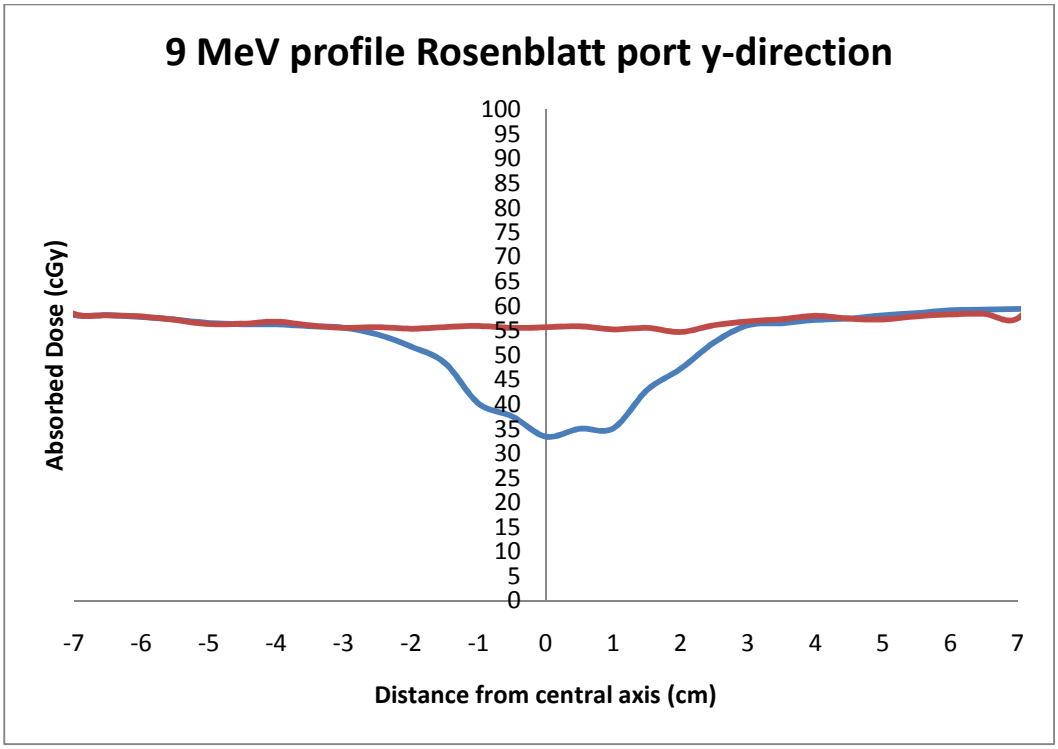

Figure 30 Rosenblatt Port 9 MeV Y-axis

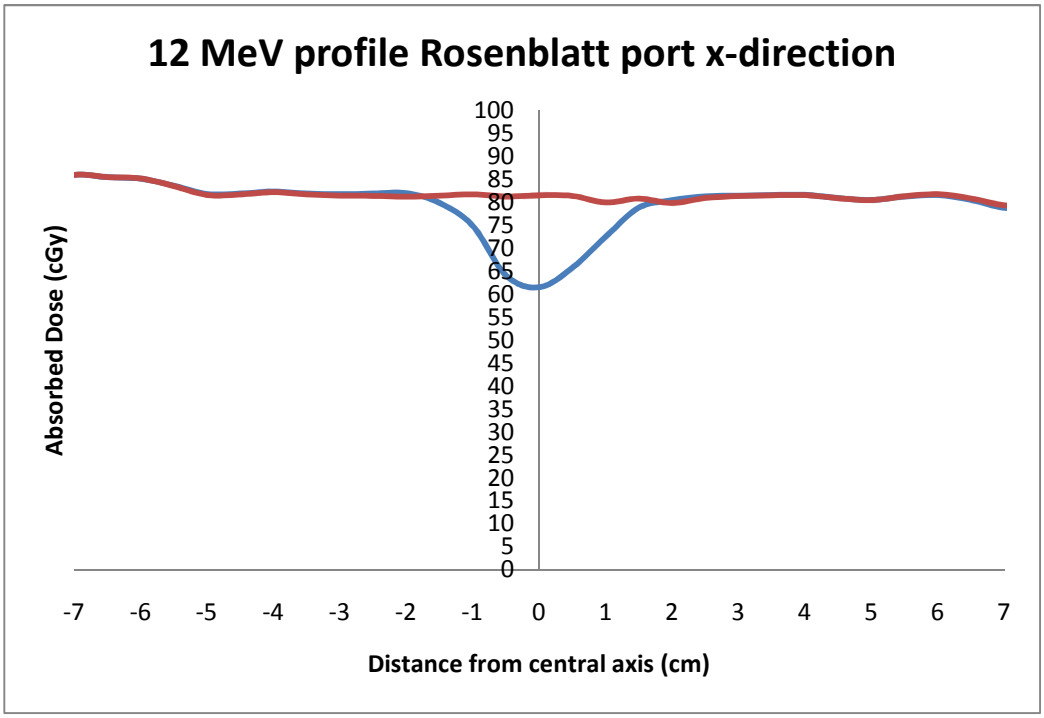

Figure 31 Rosenblatt Port 12 MeV X-axis

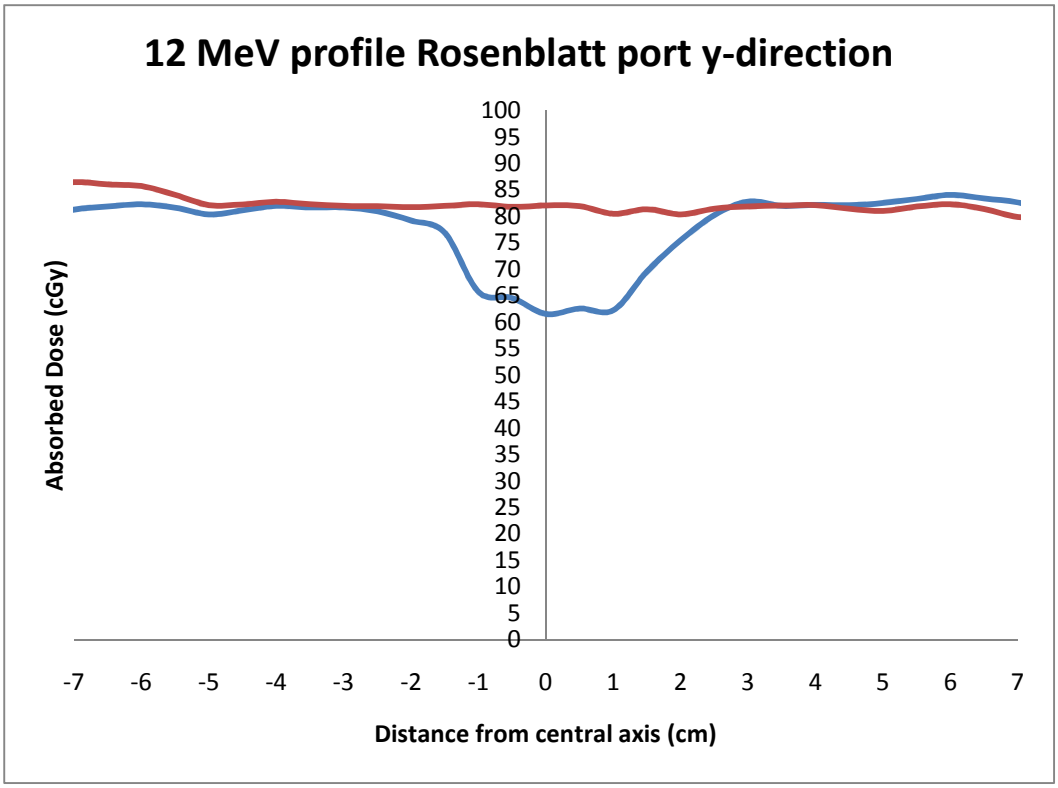

Figure 32 Rosenblatt Port 12 MeV Y-axis

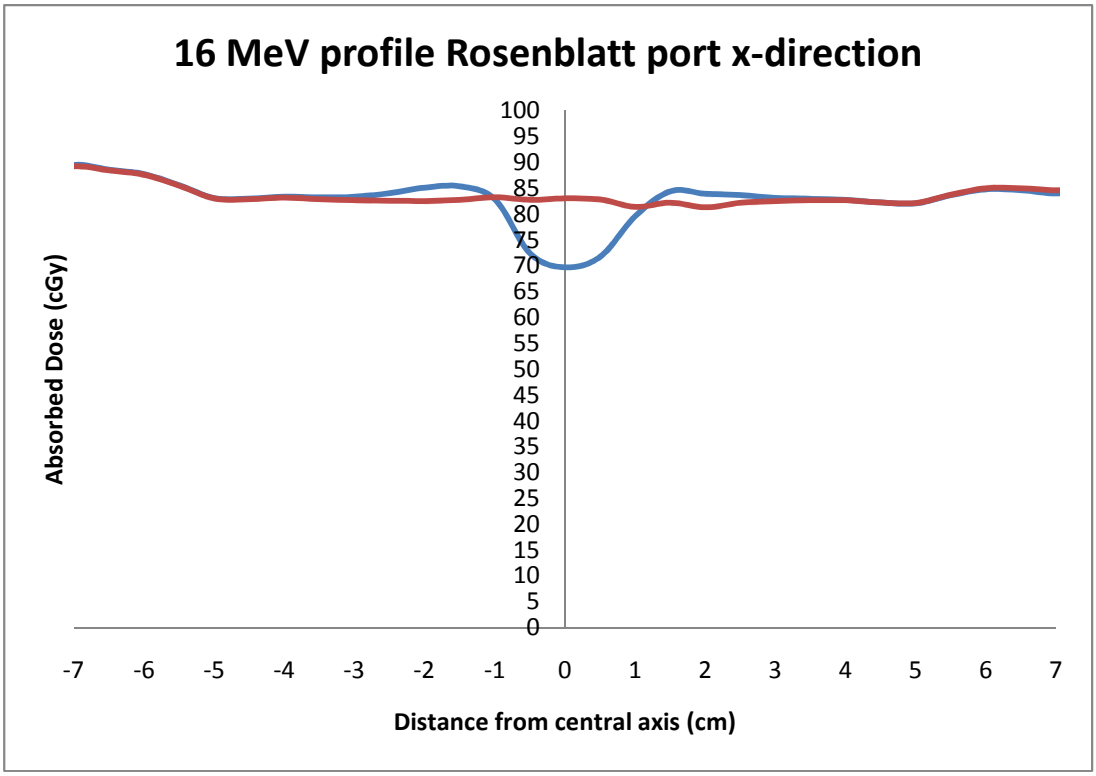

Figure 33 Rosenblatt Port 16 MeV X-Axis

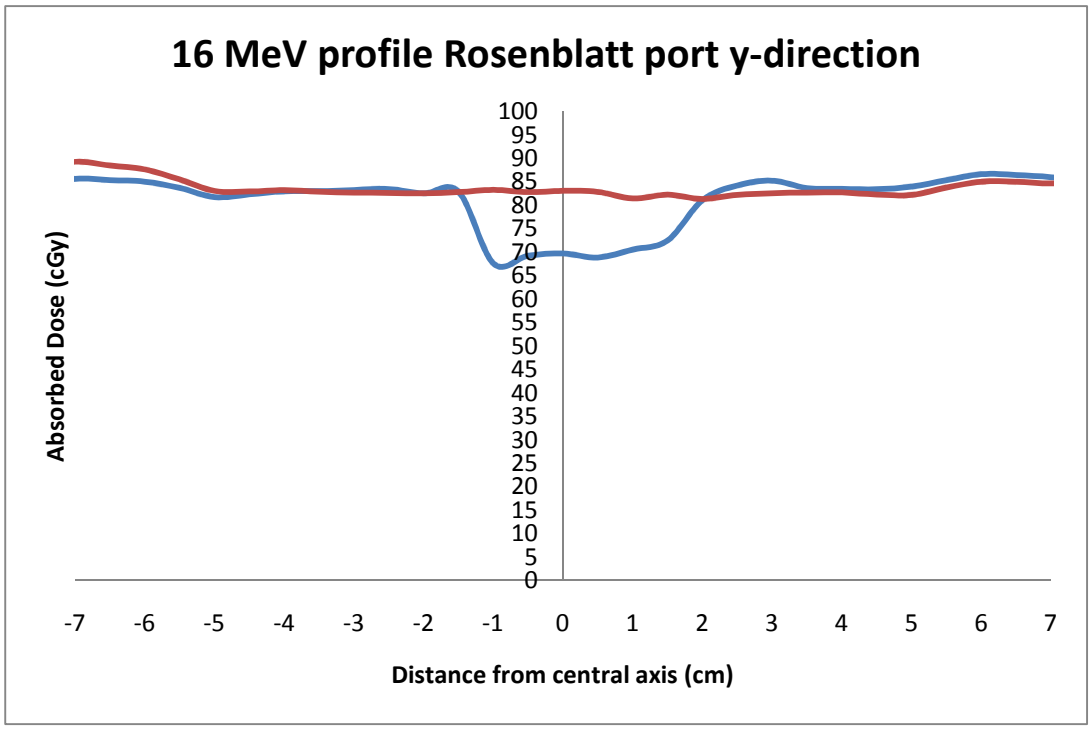

Figure 34 Rosenblatt Port 16 MeV Y-Axis

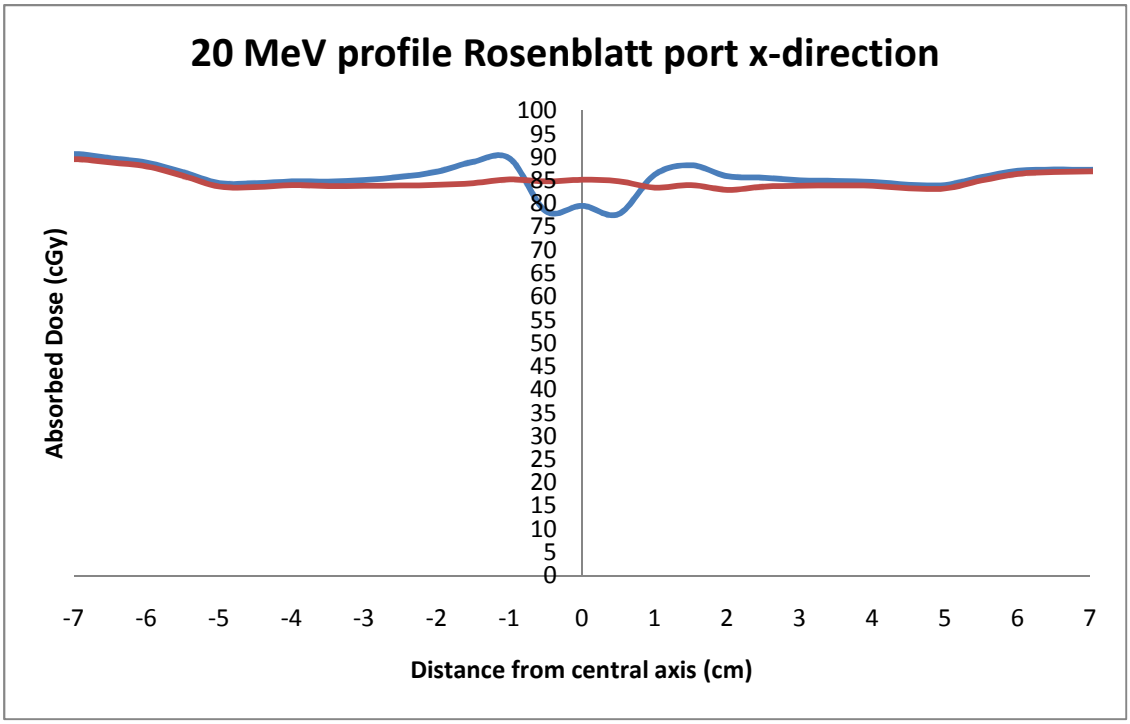

Figure 35 Rosenblatt Port 20 MeV X-axis

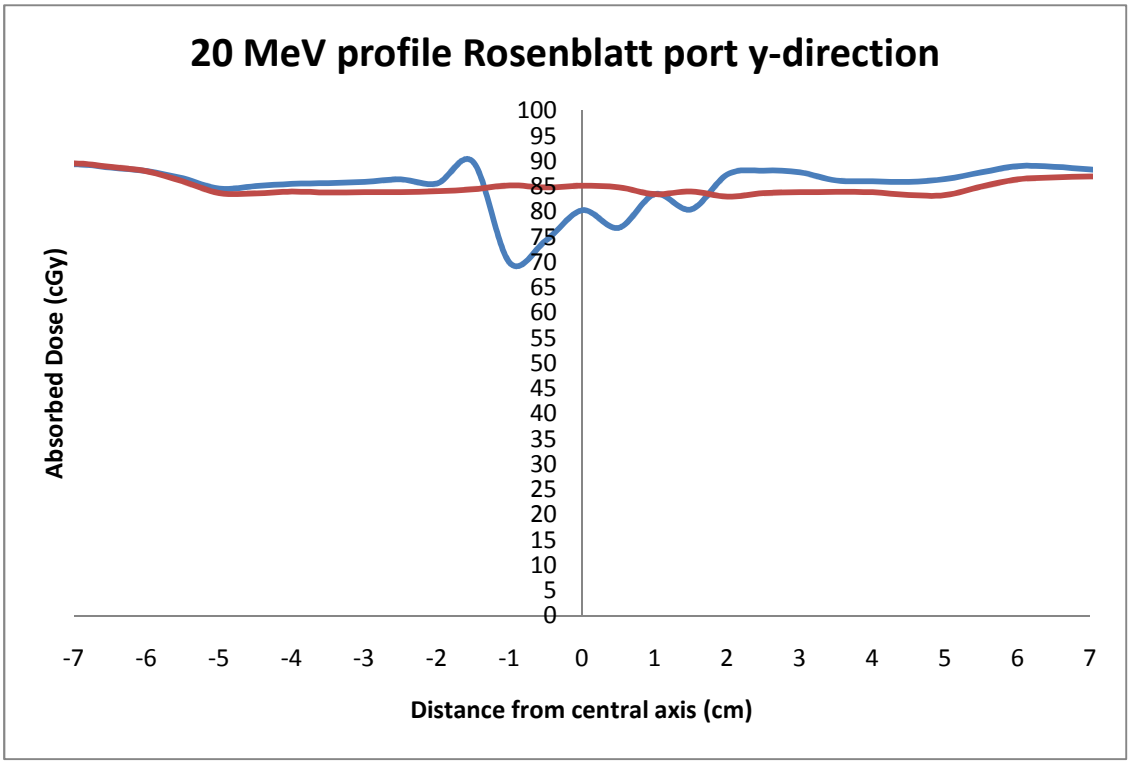

Figure 36 Rosenblatt Port 20 MeV Y-axis

Port 3: 1808000 MRI Powerport

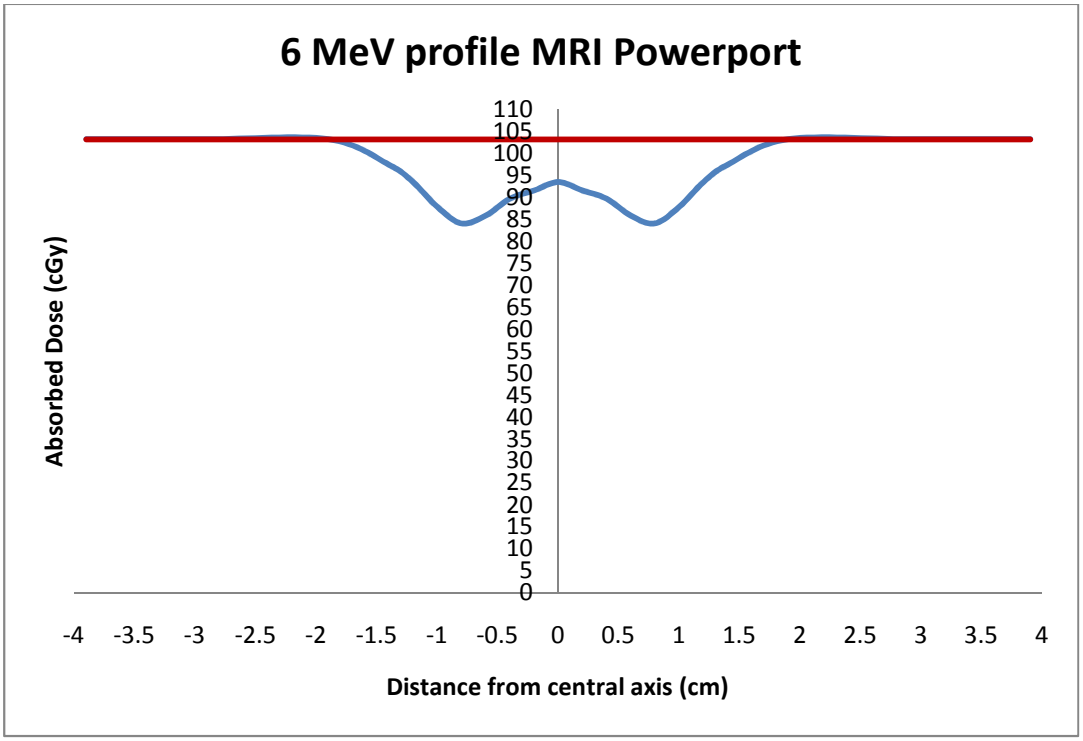

Figure 37 MRI Powerport 6 MeV

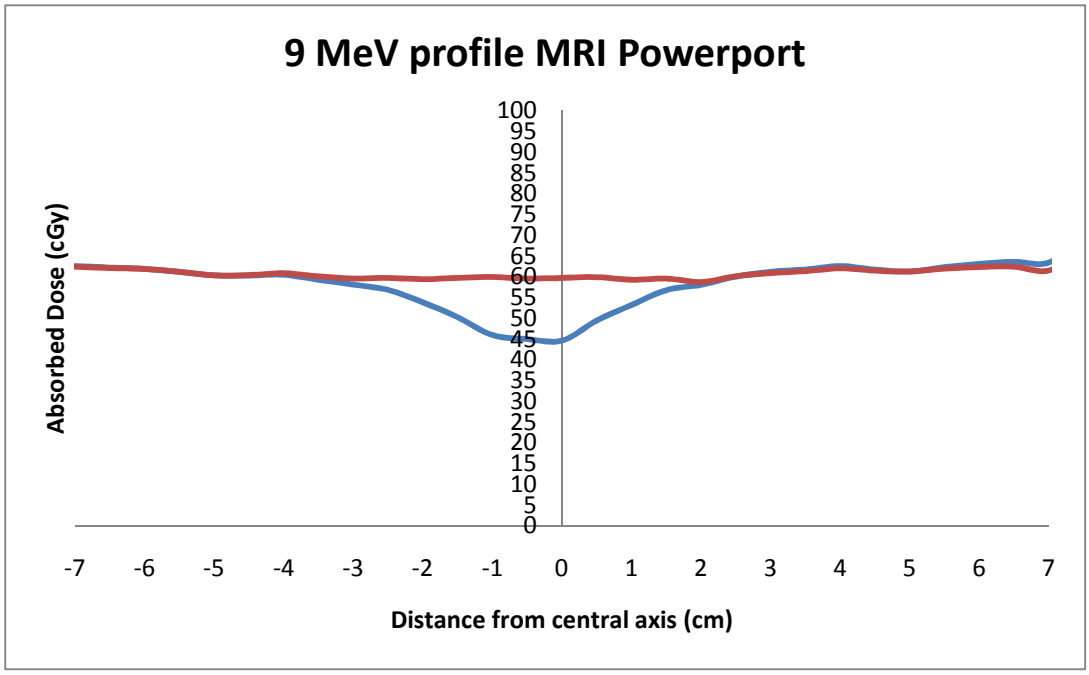

Figure 38 MRI Powerport 9 MeV

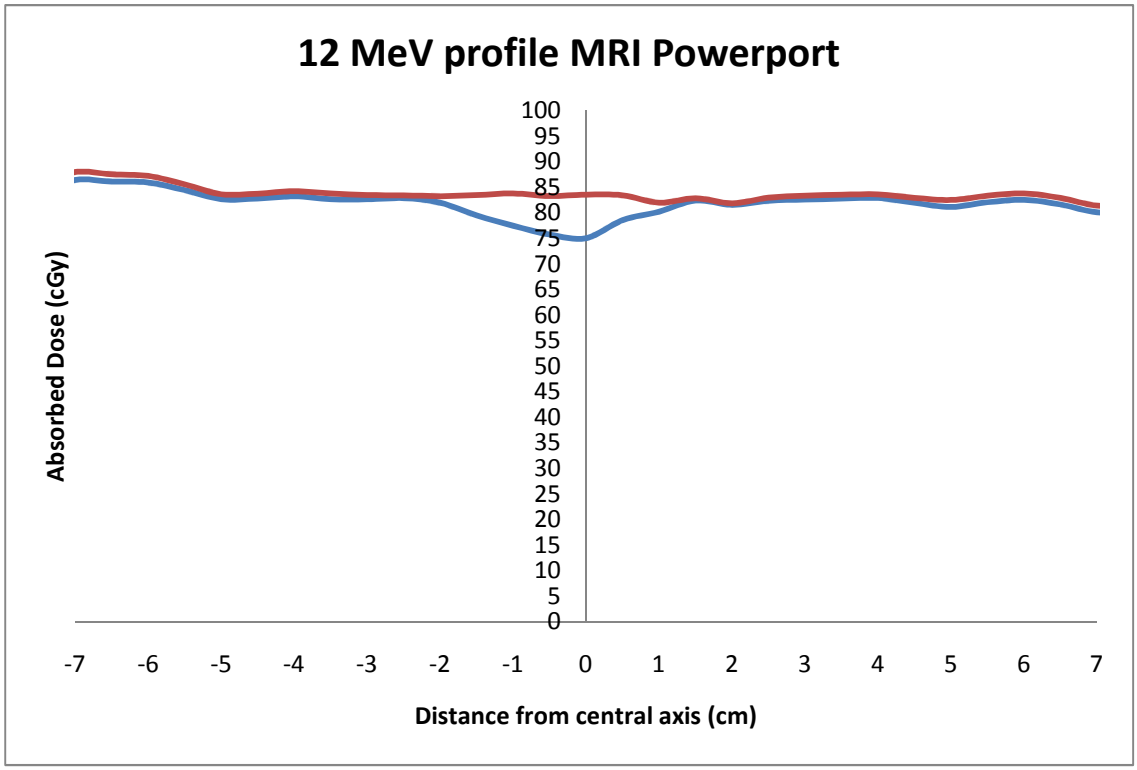

Figure 39 MRI Powerport 12 MeV

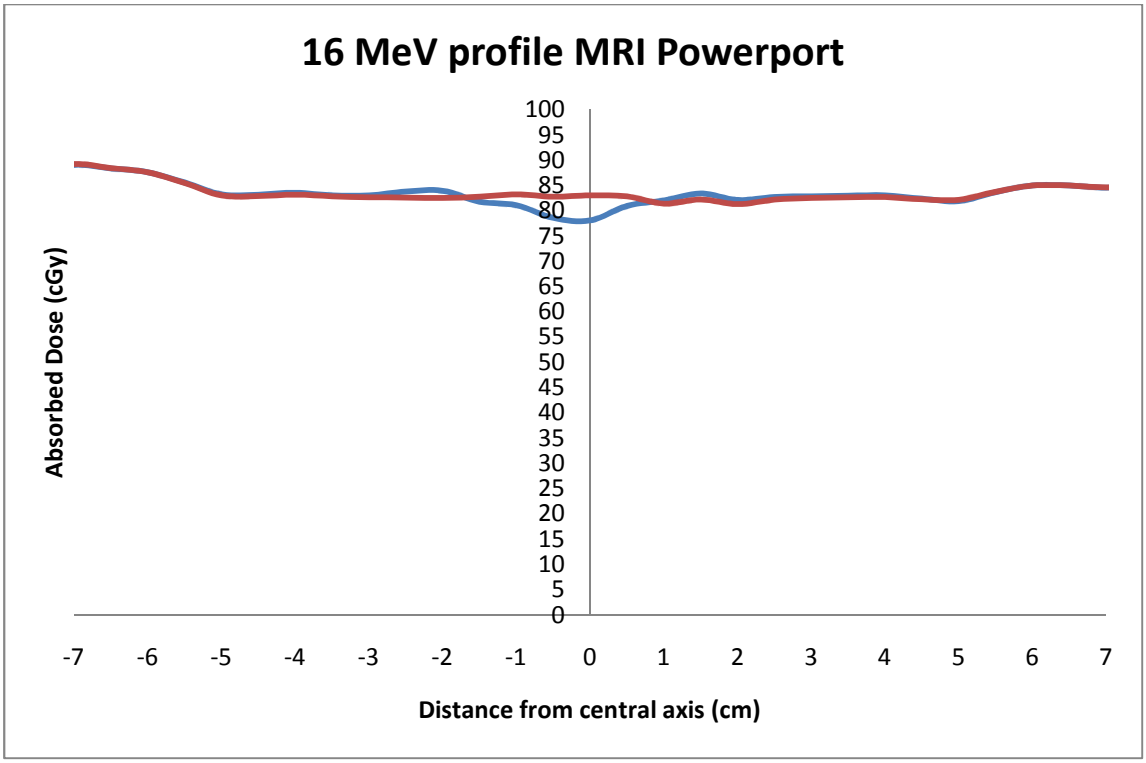

Figure 40 MRI Powerport 16 MeV

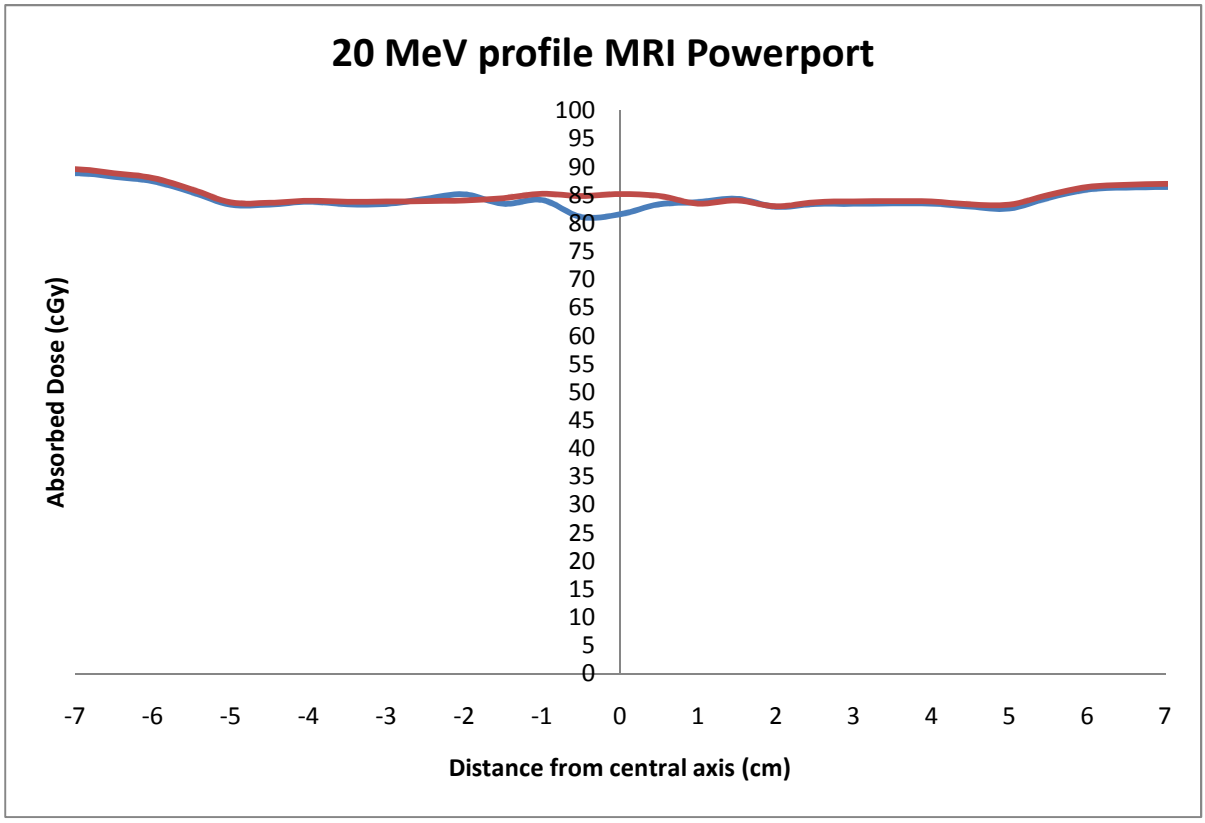

Figure 41 MRI Powerport 20 MeV

Port 4: 0655640 Ultra Low Profile

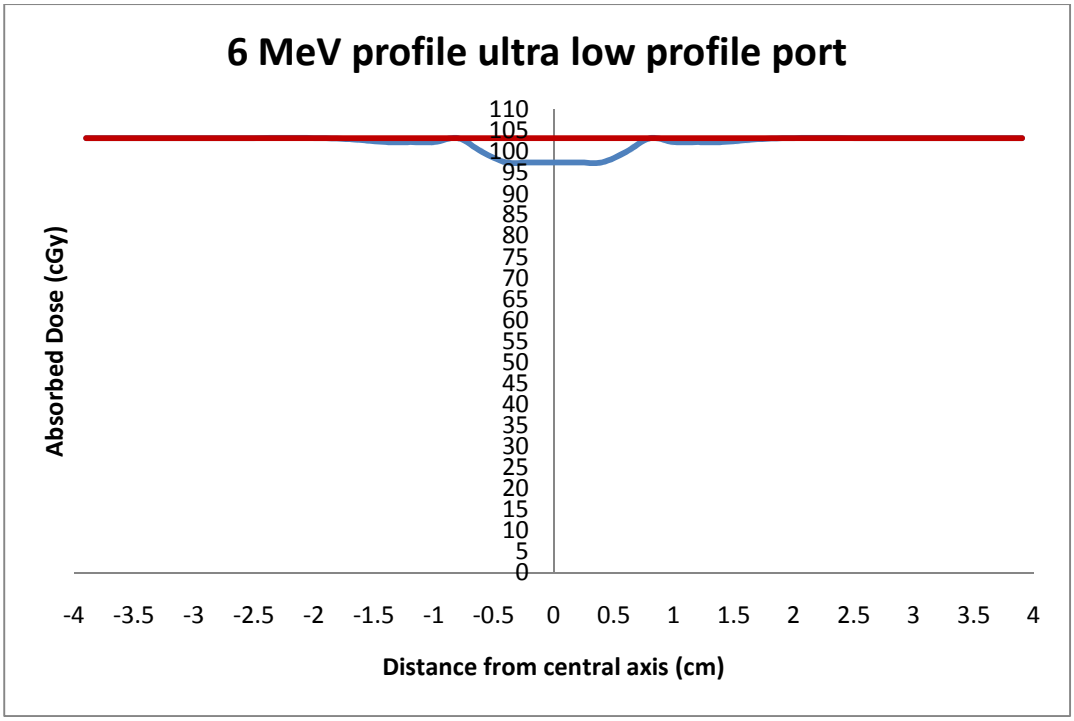

Figure 42 Ultra Low Profile Port 6 MeV

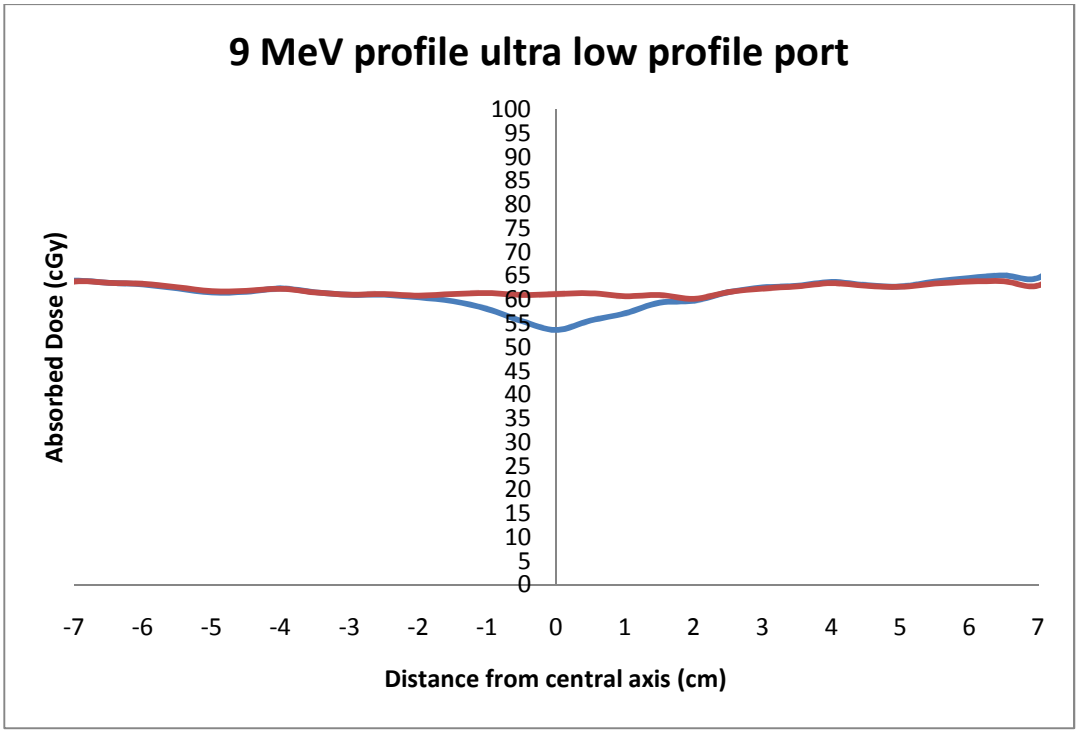

Figure 43 Ultra Low Profile Port 9 MeV

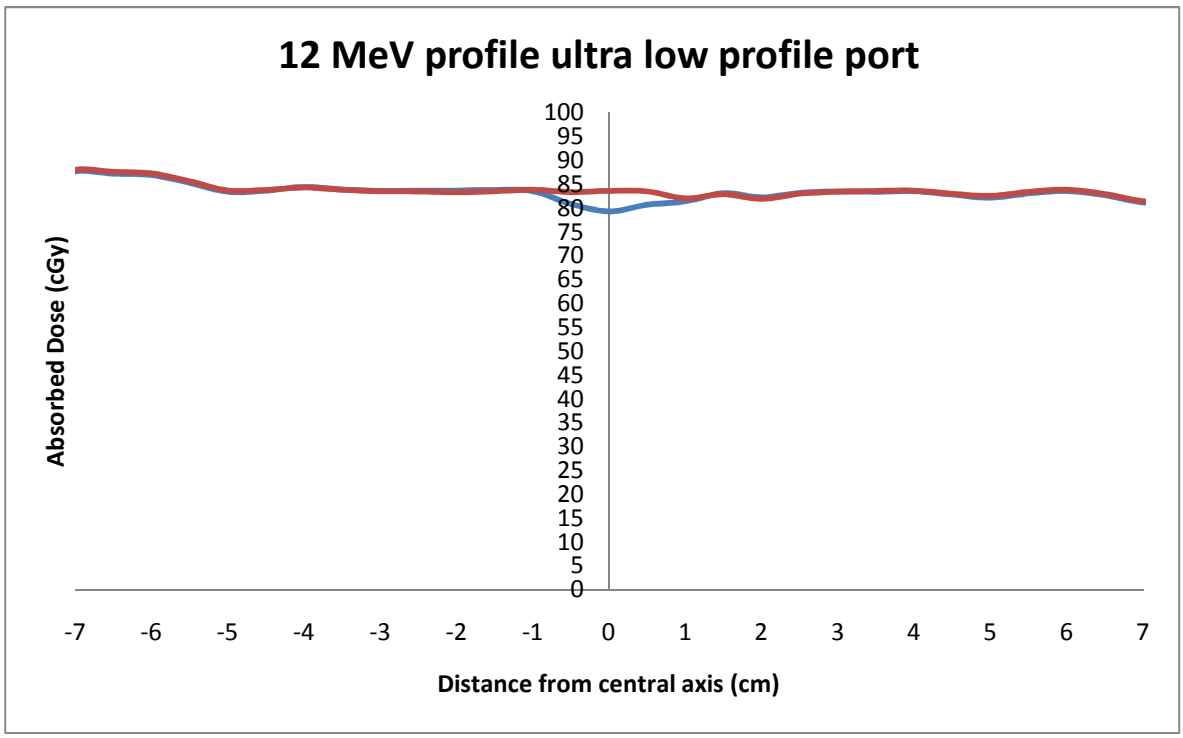

Figure 44 Ultra Low Profile Port 12 MeV

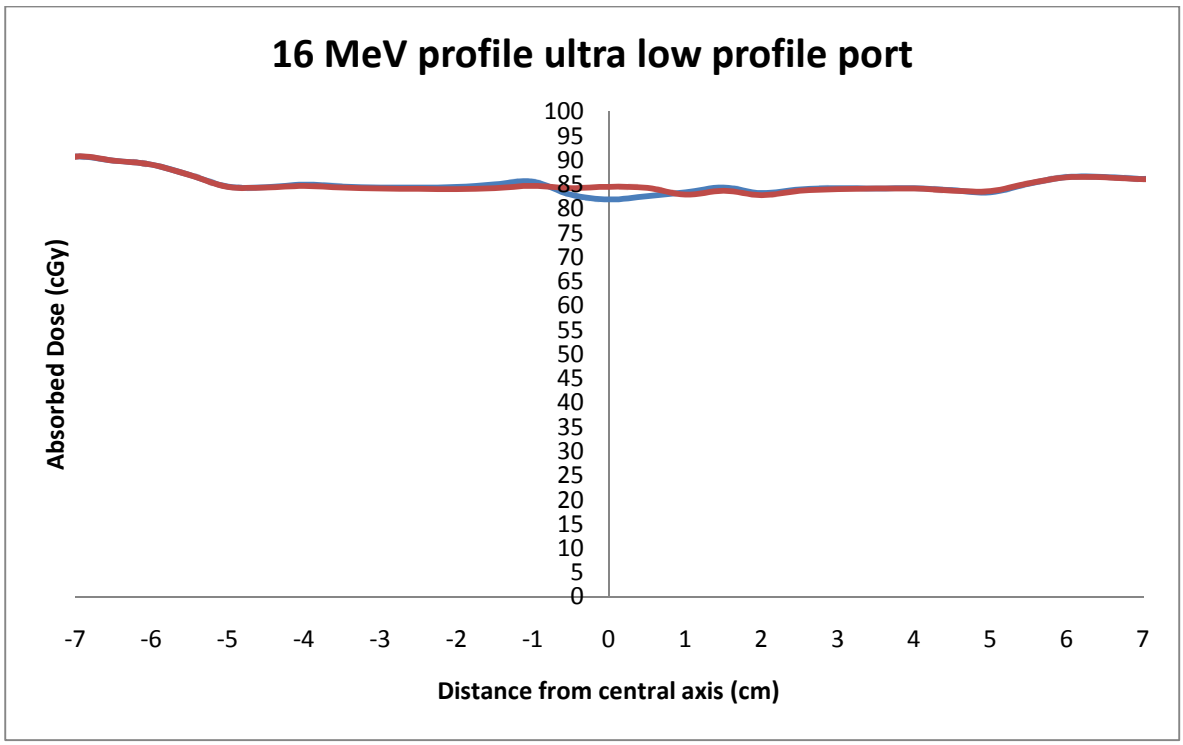

Figure 45 Ultra Low Profile Port 16 MeV

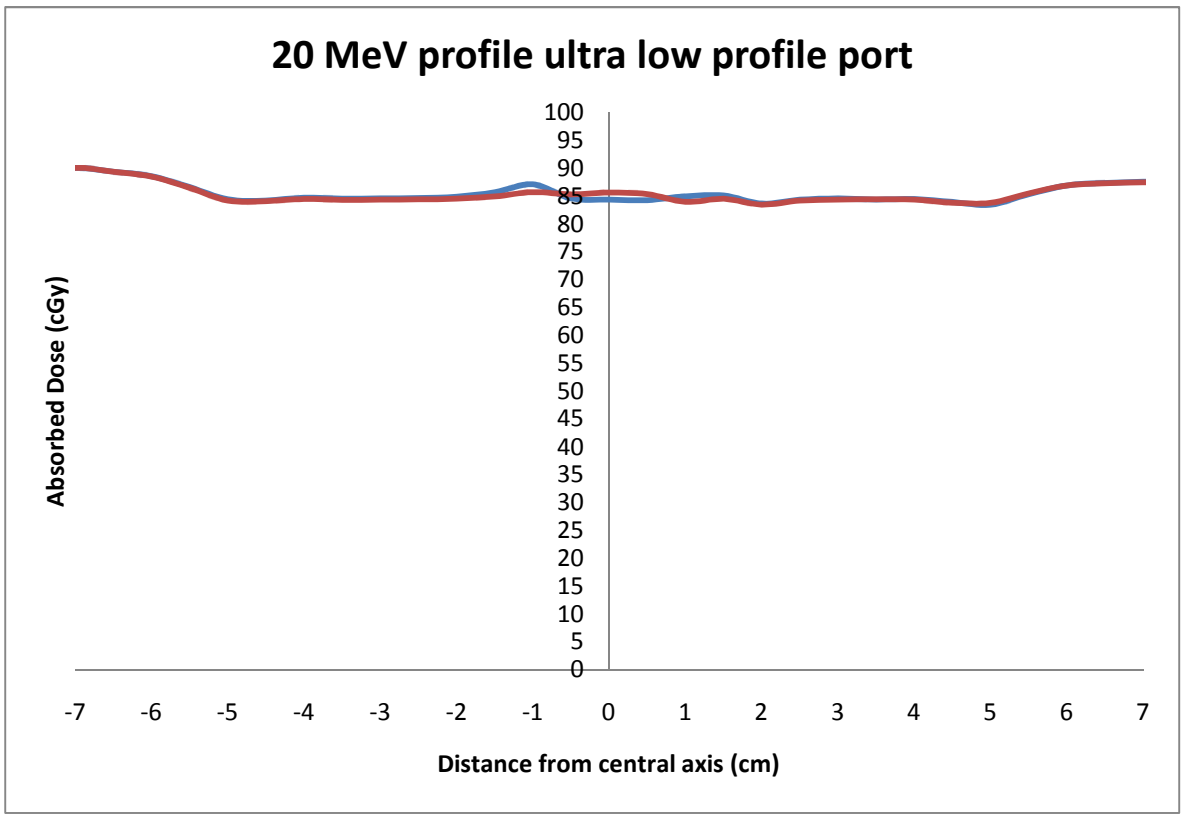

Figure 46 Ultra Low Profile Port 20 MeV

Port 5: 0607650 X-port Duo

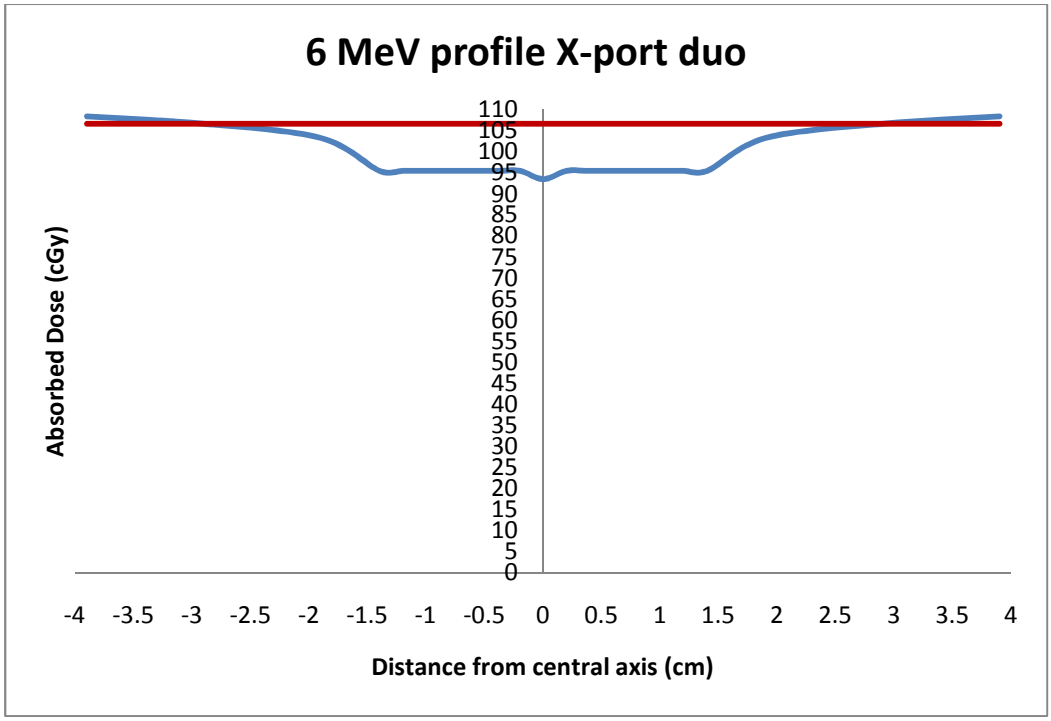

Figure 47 X-port Duo 6 MeV

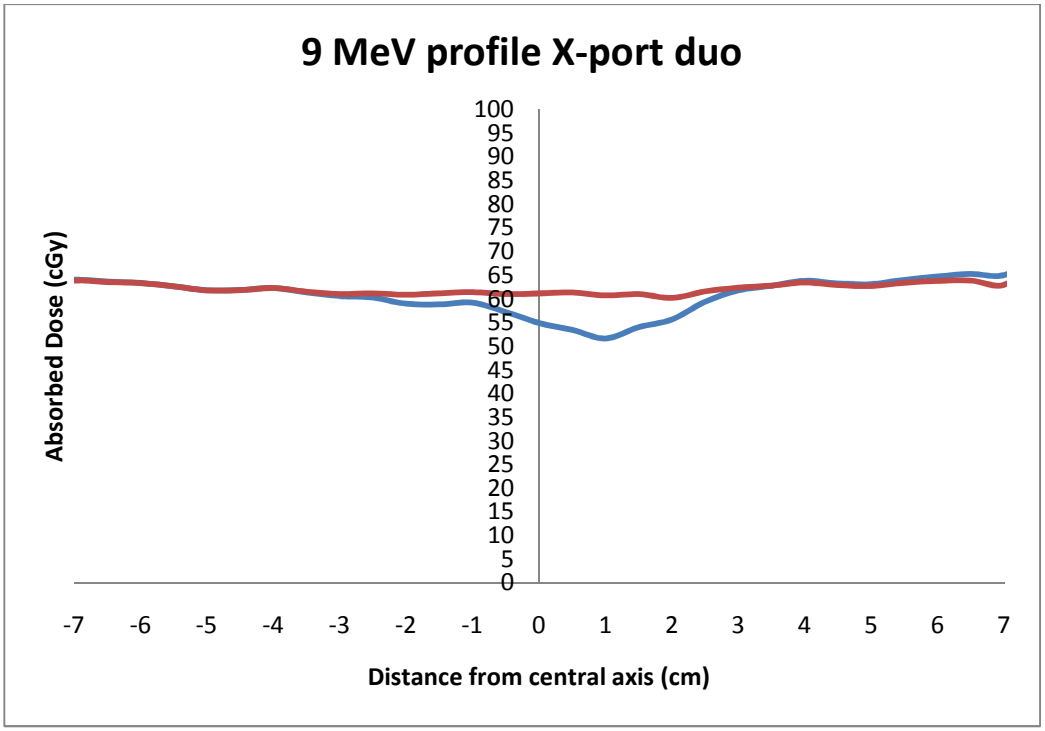

Figure 48 X-port Duo 9 MeV

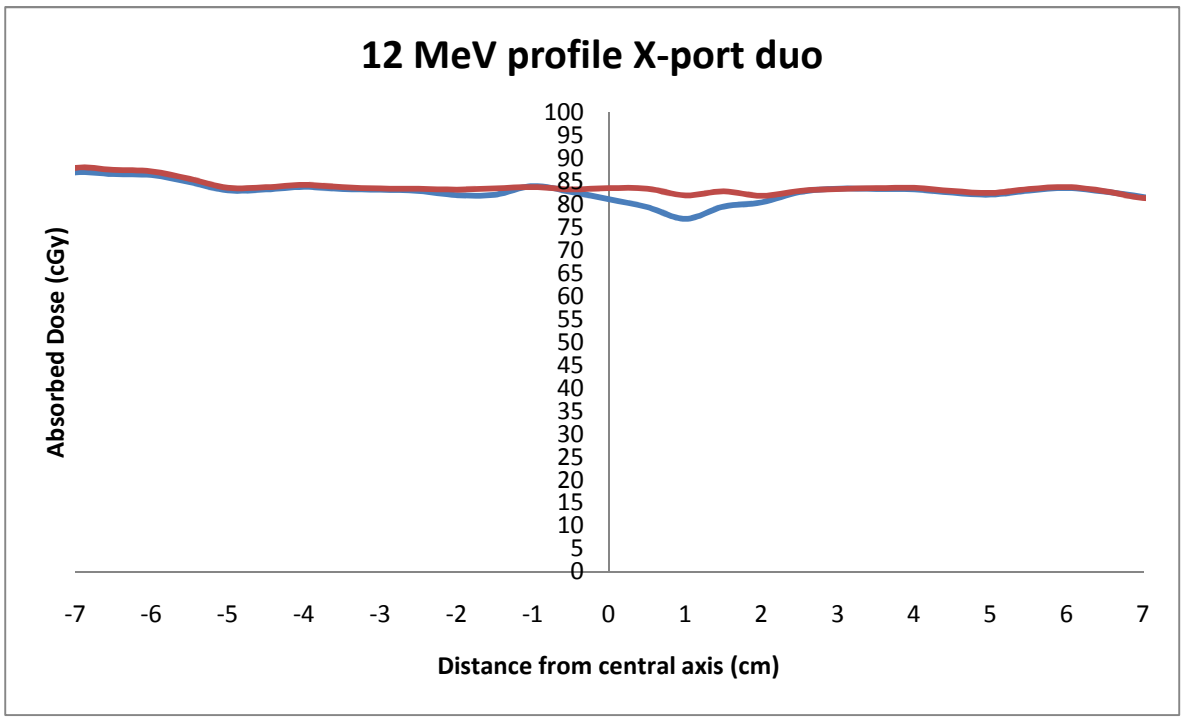

Figure 49 X-port Duo 12 MeV

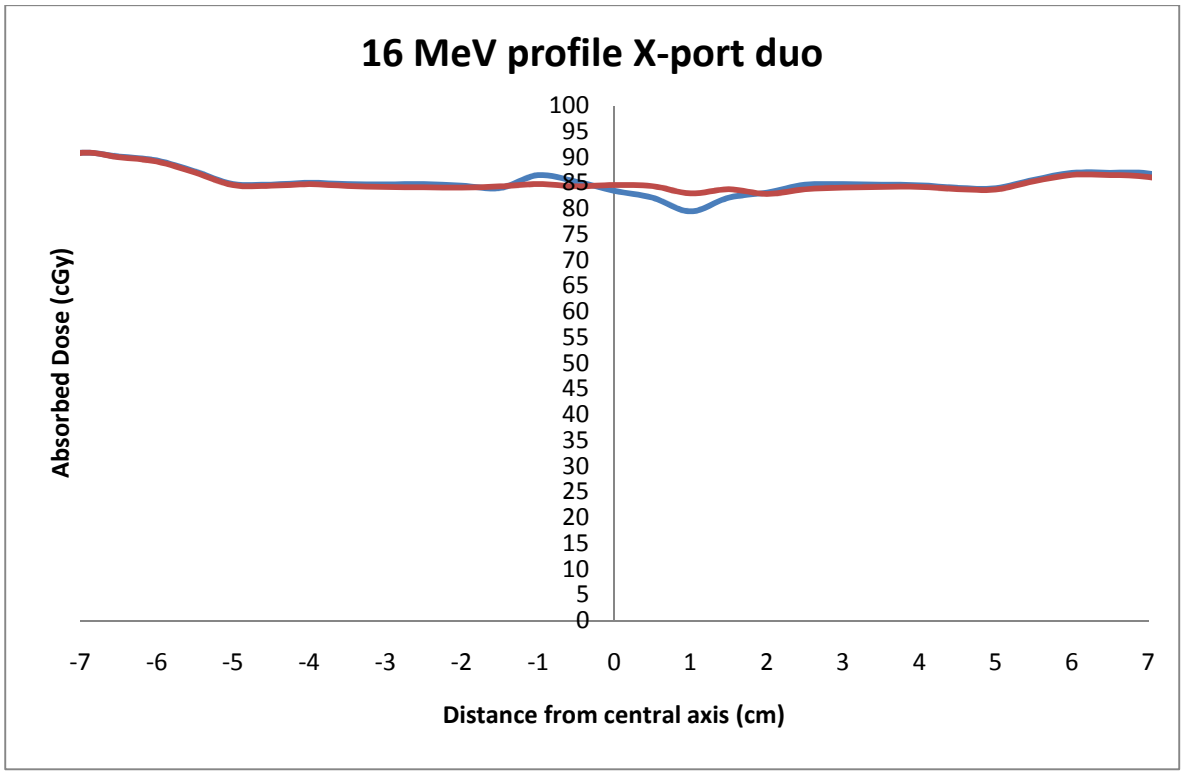

Figure 50 X-port Duo 16 MeV

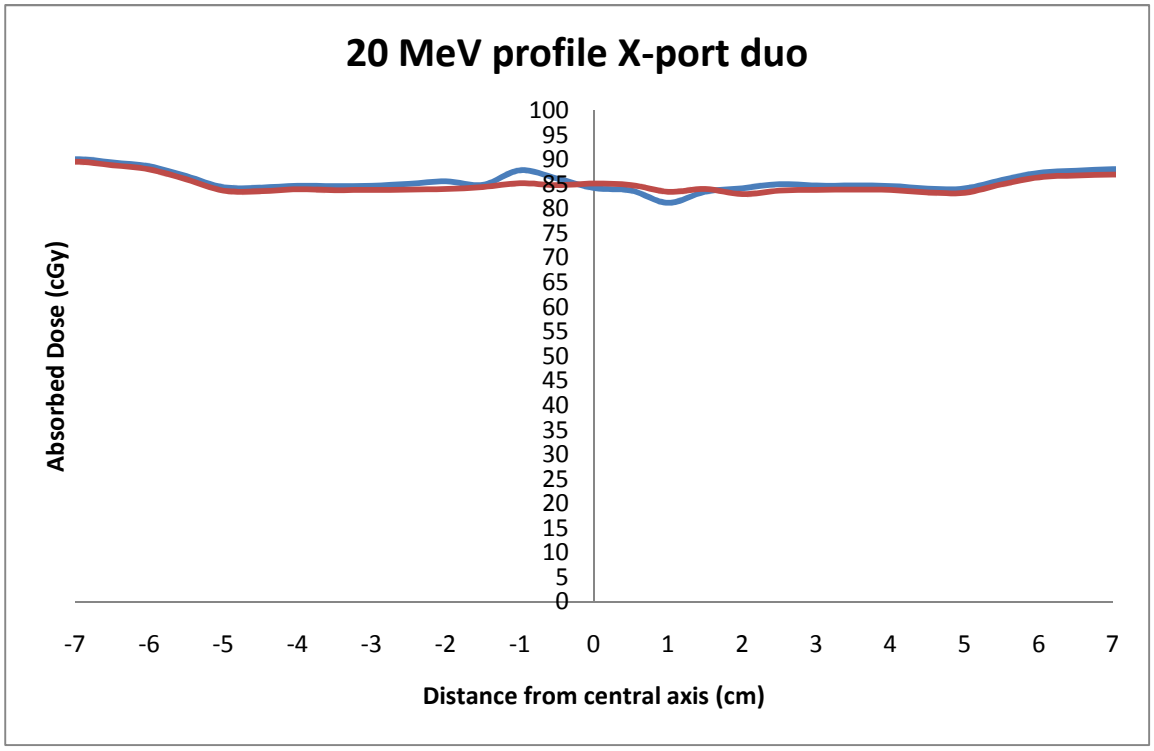

Figure 51 X-port Duo 20 MeV

Port 6: 0603880 Low Profile MRI

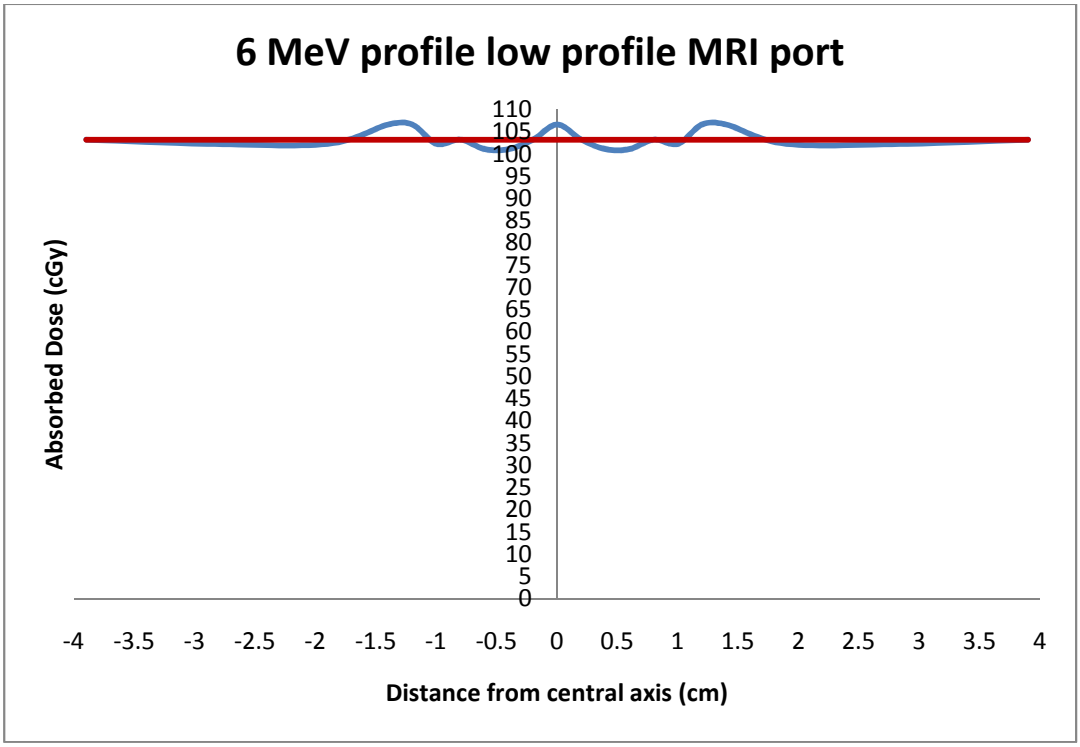

Figure 52 Low Profile MRI Port 6 MeV

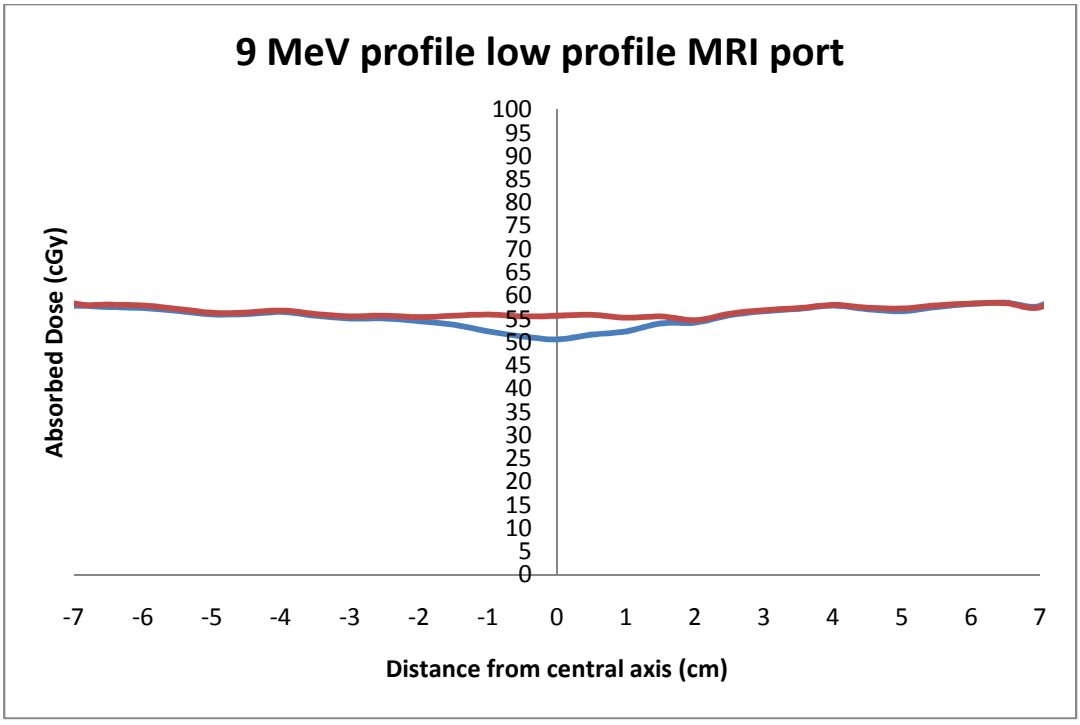

Figure 53 Low Profile MRI Port 9 MeV

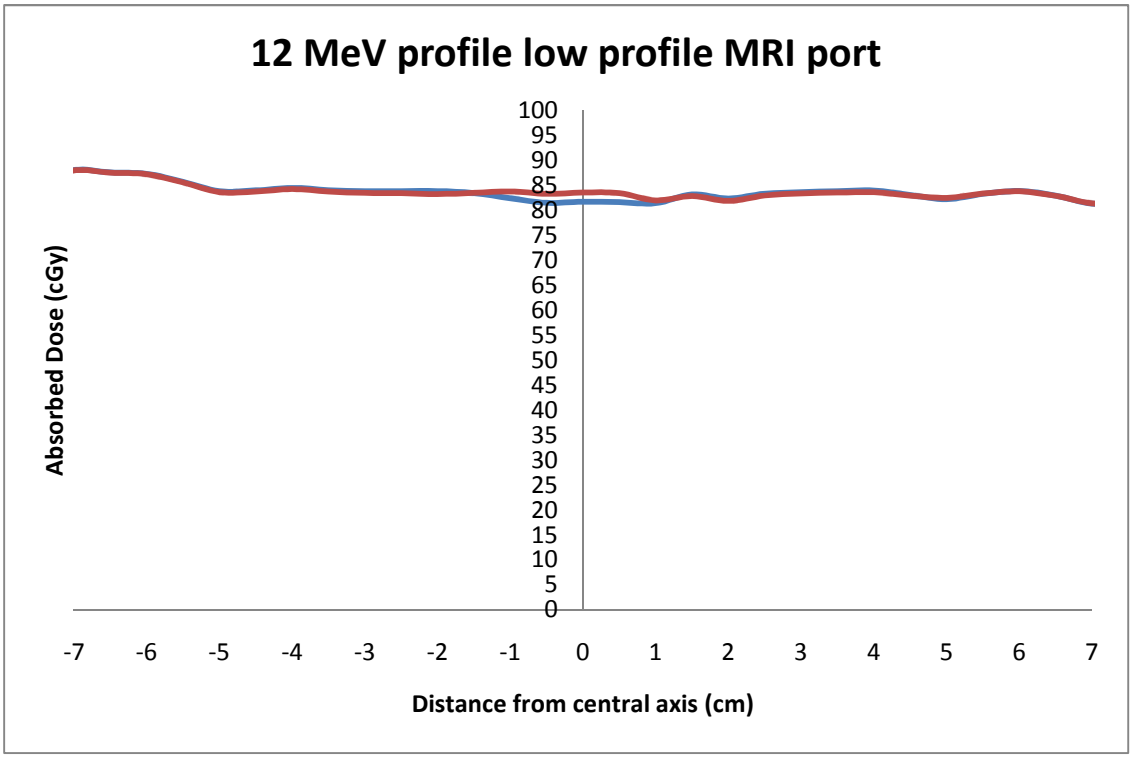

Figure 54 Low Profile MRI Port 12 MeV

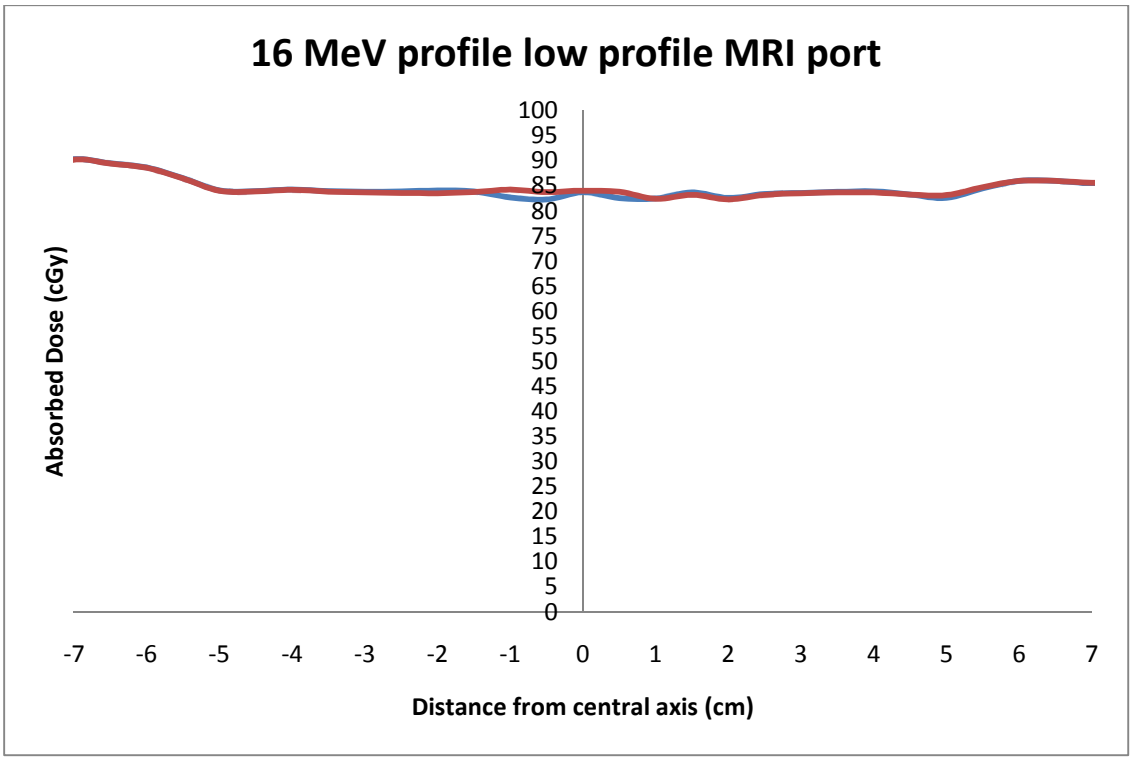

Figure 55 Low Profile MRI Port 16 MeV

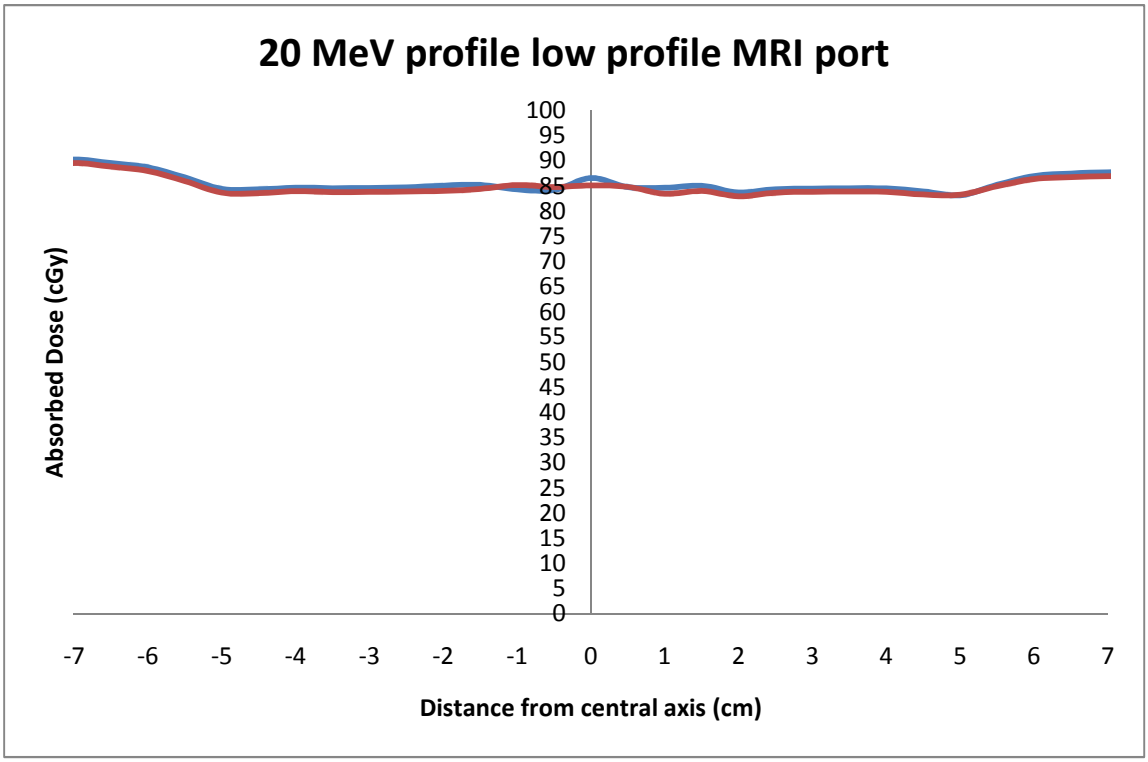

Figure 56 Low Profile MRI Port 20 MeV

Port 7: 0604520 Plastic Hard Base

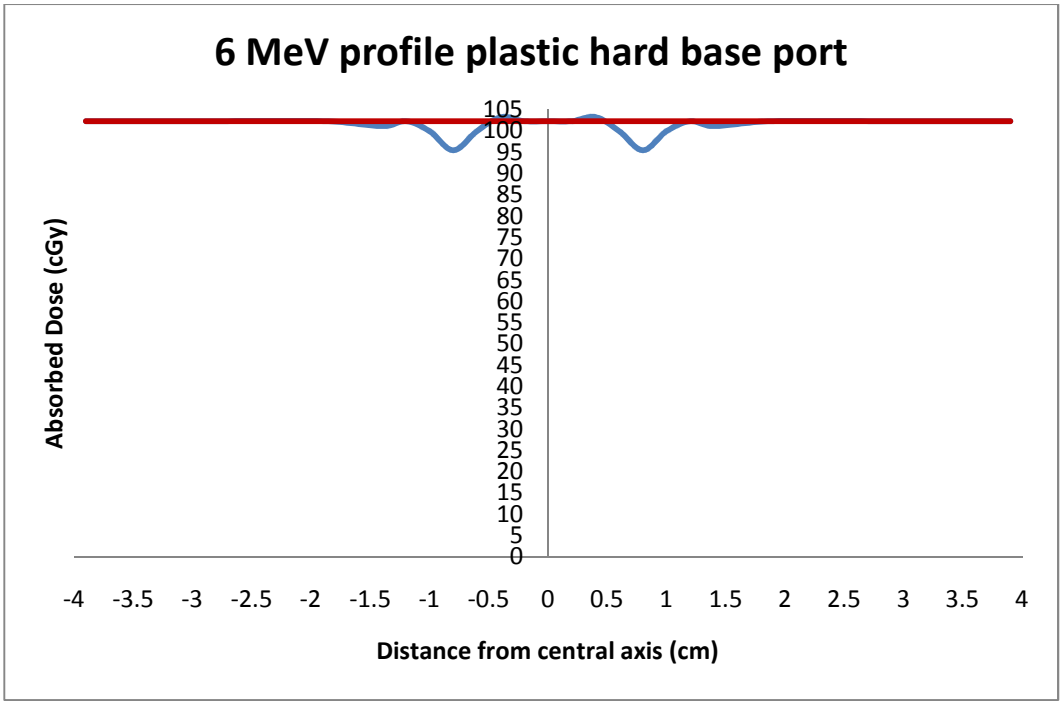

Figure 57 Plastic Hard Base Port 6 MeV

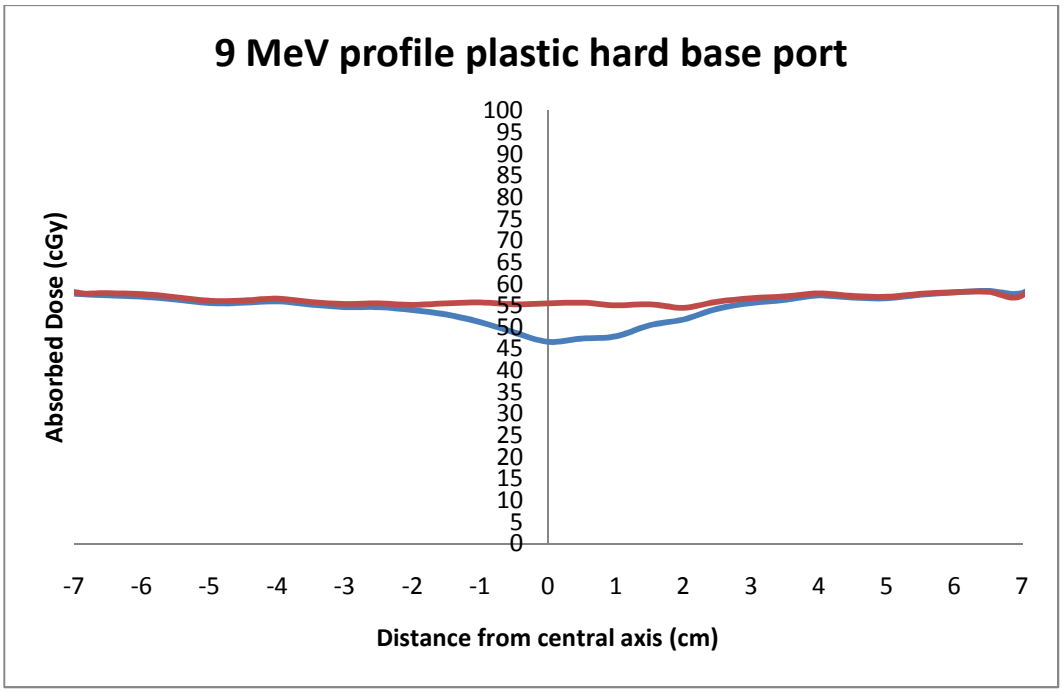

Figure 58 Plastic Hard Base Port 9 MeV

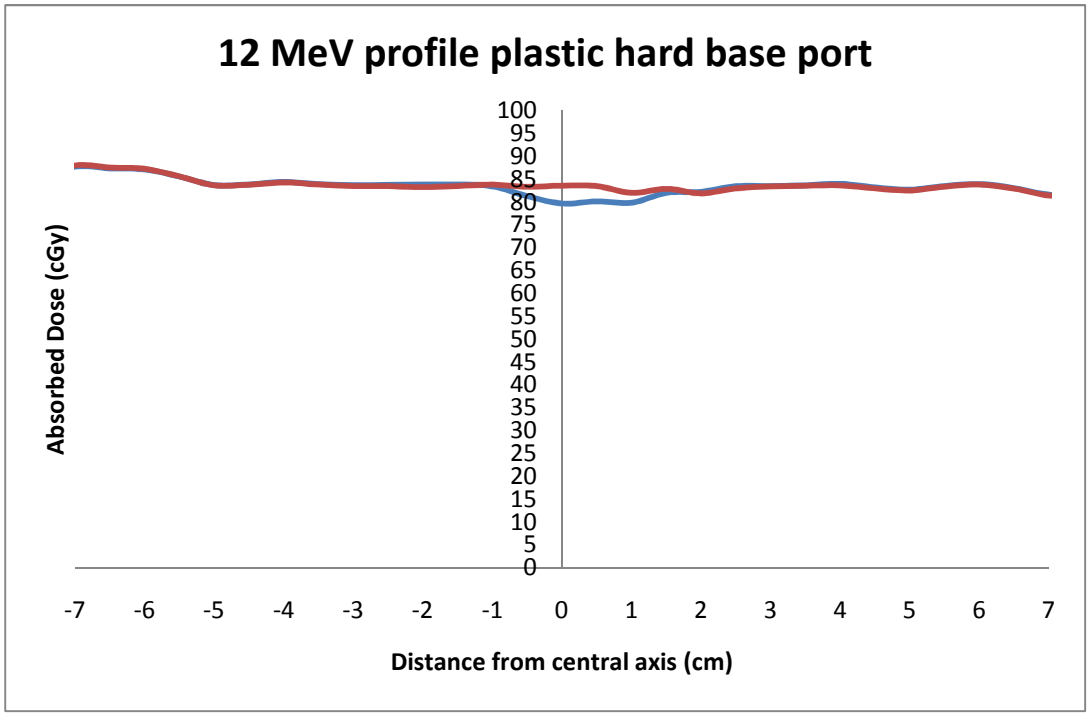

Figure 59 Plastic Hard Base Port 12 MeV

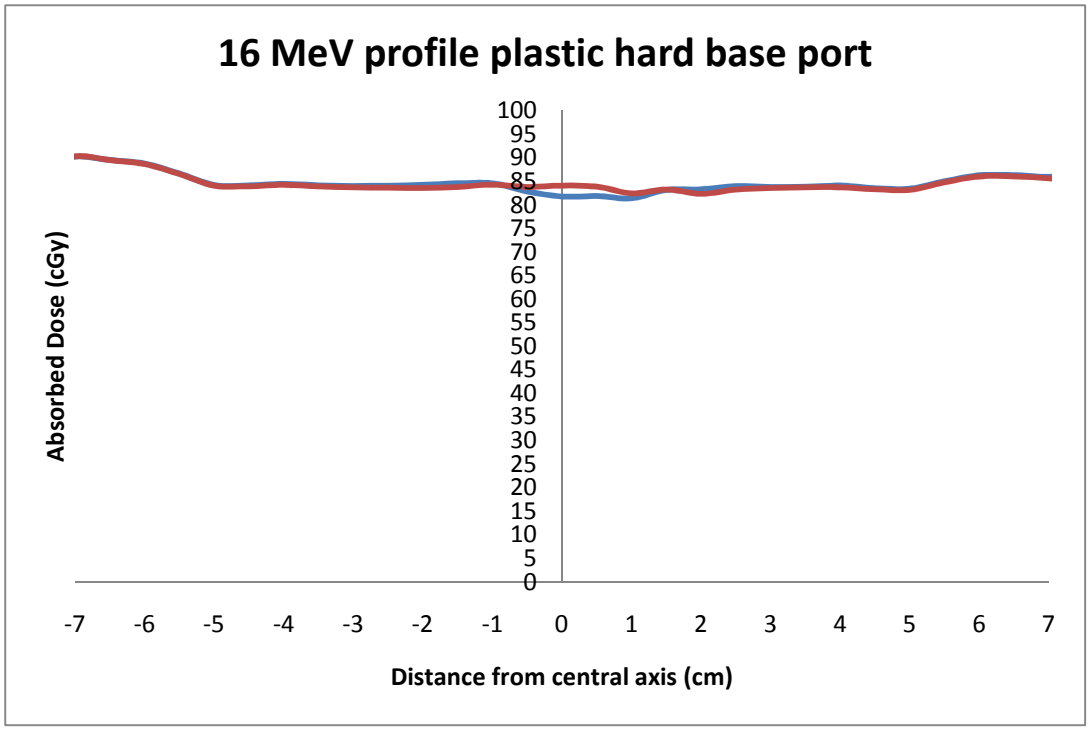

Figure 60 Plastic Hard Base Port 16 MeV

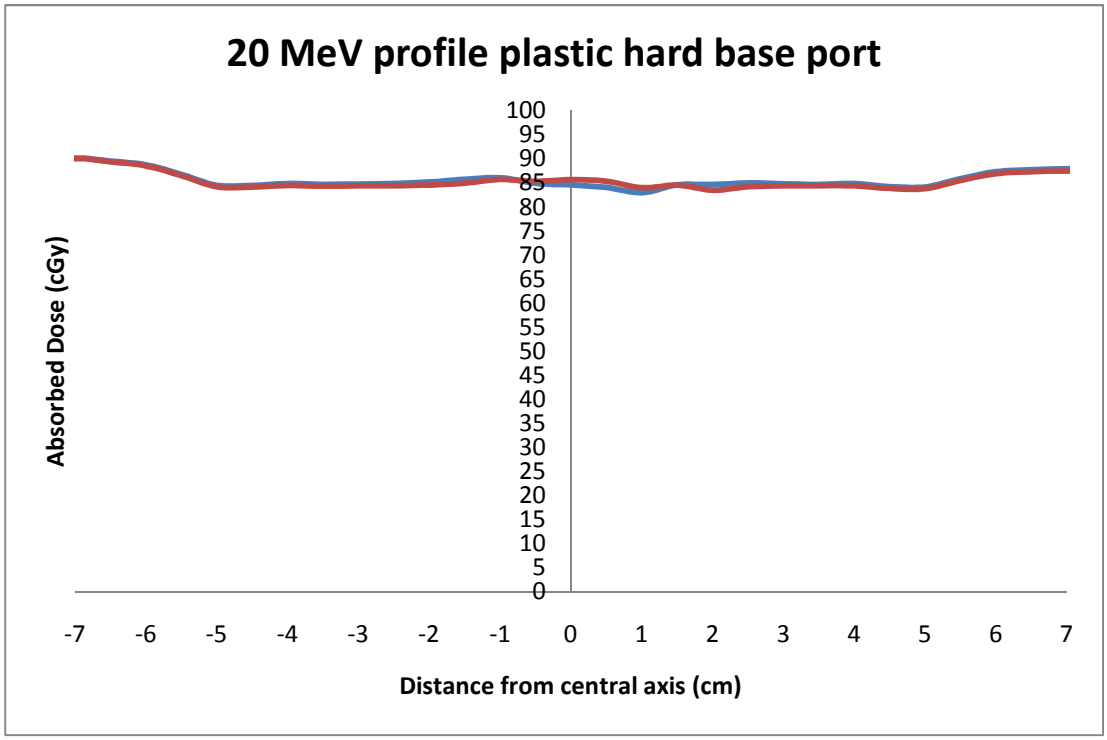

Figure 61 Plastic Hard Base Port 20 MeV

VII. REFERENCES

1. – Riley J, Garcia T and Guerrero T. *The Utilization of a 3-Dimensional Non-coplanar Treatment Plan to Avoid Pacemaker Complication.* Med Dos 2003:29**;**92-96.

2.- Gossman MS, Graves-Calhoun AR, Wilkinson JD. *Establishing Radiation Therapy Treatment Planning Effects Involving Implantable Pacemakers and Implantable Cardioverter-Defibrillators*. J of Applied Clinical Medical Phys. 2010:11(1):33-45

3. - Gossman MS. Personal Interview. September 14, 2010.

4.- Dillon PA, Foglia RP. *Complications Associated With an Implantable Vascular Access Device*. Journal of Pediatric Surgery. 2006:41:1582-1587

5.- Goodman MS, Wickham R. *Venous Access Devices: an overview*. Oncology Nursing Forum, 1984:11(5): 16-23

6.- Kelly L. *The Family of Vascular Access Devices*. Journal of Infection Prevention. September 2, 2009;10(S1):s7-s12

7.- Bagne FR, Merrick HW 3rd, Samsami N, and Dobelbower RR Jr. *Radiation Dose Perturbation in the Presence of Permanent Vascular-Access Injection Ports*. Int J Rad Oncol Biol Phys. 1990;18(2):463–67.

8.- Gossman MS, Seuntjens JP, Serban MM, Lawson RC, Robertson MA, Lopez JP, Justice TE. *Dosimetric Effects Near Implanted Vascular Access Ports: an Examination of External Photon Beam Dose Calculations*. J of Applied Clinical Medical Phys. 2009:10(3):3-15

9.- Zhao L, Cheng CW, Moskvin V, Wolanski M, James J, Gossman MS, Dikeman K, Srivastava S, and Das IJ. *Dose Uncertainty Due to High-Z Materials in Clinical Proton Beam Therapy*. American Association of Physicists in Medicine, Philadelphia, PA, 2010.

10.- Delacroix S, Rymel J, Smith PJ, Clubb BS. *The Effects of Steel and Titanium Mandibular Reconstruction Plates on Photon and Electron Beams*. The British Journal of Radiology. 1990: 63: 642-645

11.- Lin SY, Chu TC, Lin JP, Liu MT. *The Effect of a Metal Hip Prosthesis on the Radiation Dose in Therapeutic Photon Beam Irradiations.* Applied Radiation and Isotopes 2002:57:17-23

12.- Onders R, Shenk R, Stellato T. *Long-term Central Venous Catheters: Size and Location Do Matter*. American Journal of Surgery. March 2006;191(3):396-399

13.- Kahn FM, Doppke KP, Hogstrom KR, Kutcher GJ, Nath R, Prasad SC, Purdy JA, Rozenfeld M, Werner BL. *Clinical Electron-Beam Dosimetry: Report of AAPM Radiation Therapy Committee Task Group No. 25*. Med Phys 1991: 18 (I): 73-109

14.- Hogstrom KR, Almond PR. *Review of Electron Beam Therapy Physics*. Phys Med Biol 51. 2006: R455-R489

15.- Kahn, FM. *The Physics of Radiation Therapy (3rd edition)* Lippincott Williams & Wilkins, 2003

16.- Hendee WR, Ritenour ER. *Medical Imaging Physics (4th edition)* Wiley-Liss, Inc. New York (2002)

17.- Johns HE and Cunningham JR. *The Physics of Radiology (4th Ed.).* Charles C. Thomas Publishing, Springfield, IL, 1983, pp. 67